remote sensing

MDPI

Article

Weather-Dependent Nonlinear Microwave Behavior of Seasonal High-Elevation Snowpacks

Yueqian Cao, and Ana P. Barros*

Department of Civil and Environmental Engineering, Duke University, Durham, North Carolina, USA;

*Correspondence: barros@duke.edu

Received: ××; Accepted: ××; Published: ××

Abstract: Ensemble predictions of the seasonal snowpack over Grand Mesa, CO were conducted for the hydrologic year 2016-2017 using a multilayer snow hydrology model. Ensembles were generated from gridded atmospheric reanalysis, model predictions were evaluated against SnowEx'17 measurements, and the signatures of the weather-dependent variability of snow physics in the behavior of multi-frequency microwave brightness temperatures and backscattering were examined through forward modeling. At sub-daily time-scales, the ensemble standard deviation due to atmospheric forcing (i.e., mesoscale spatial variability of weather within the Grand Mesa) is < 3 dB for dry snow, and increases to 8-10 dB at mid-day when there is surficial melt that also explains the wide ensemble range (~20 dB). Further, the ensemble mean backscatter exhibits robust (R^2 > 0.95) time-varying, weather-dependent linear heuristic relationships with SWE (e.g., 5-6 cm/dB/month in January; 2-2.5 cm/dB/month in late February) as melt-refreeze cycles modify the microphysical structure in the top 50 cm of the snowpack. The nonlinear evolution of ensemble snow physics translates into seasonal hysteresis in the microwave behavior. The backscatter hysteretic offsets between accumulation and melt regimes are robust in the L- and C-bands and collapse for wet shallow snow at Ku-band. The ensemble mean emissions behave as a limit-cycles with weak sensitivity in the accumulation regime, and hysteretic behavior during melt that is different for deep (winter-spring transition) and shallow snow (spring-summer) and offsets that increase with frequency. These findings suggest potential for multi-frequency active-passive remote-sensing of SWE conditional on snowpack regime, particularly suited for data-assimilation using coupled snow hydrology-microwave models.

Keywords: seasonal snow; hydrometeorology; SWE; remote-sensing; microwave hysteresis

1. Introduction

Snow plays an important role governing the surface energy and water budgets at high elevations and over large regions of the world at high and even at mid latitudes depending on time of the year. Monthly mean snow cover varies from 7% to 40% over the Northern Hemisphere [1] and changes in snow cover due to interannual variability and increasing surface air temperatures affect not only regional atmospheric conditions but also large-scale circulation systems including the global monsoons [2-5]. The water mass stored in seasonal snowpacks can be inferred from snow covered area, snow depth and snow water equivalent (SWE) metrics. In cold regions and in high mountains, winter snowpacks temporarily

store freshwater that is subsequently released during melting, and thus modulate the availability of water resources [6,7]. The large spatial variability of precipitation, clouds, winds and land-cover translates into large spatial variability in snow accumulation patterns (snow depth and SWE) and snowpack microphysical properties. Temperature, grain size, and material composition (ice, liquid water content, and particles such as dust or pollution) determine local snowpack surface radiative properties, including emissivity and backscattering behavior, that are spatially organized by topography and land-cover at the meso- and regional scales [8,9].

Remote sensing has long been the primary strategy for large-scale monitoring of snow because of the challenges of access to high remote mountain areas and cold regions generally [10-12]. Since the 1970s, passive microwave satellite observations have been widely used to map areal snow cover and to estimate snow depth and SWE. Hall et al. [13,14] lead the first studies to establish the proposition of passive microwave remote sensing of snow that became possible with the launch of microwave radiometers onboard Nimbus 5-6-7 satellites. Rango et al. [15] identified a linear regression equation between microwave brightness temperature (18 GHz and 37 GHz, H- polarization) and snow depth, and demonstrated how the rapid increase of brightness temperatures in the spring can be used as a robust indicator of liquid water presence and the onset of the melting regime. Chang et al. [16] followed [15] to produce SWE maps over the Northern Hemisphere based on dual-polarization brightness temperature measurements from the Scanning Multichannel Microwave Radiometer (SMMR). Subsequently, Grody and Basist [17] used measurements from the next generation radiometer, the Special Sensor Microwave Imager (SSM/I) to map global snow cover. The relationship between SWE and SSM/I brightness temperatures over 16 land-cover categories was examined by Tait [18] who reported that SWE could be estimated with 95% confidence in smooth non-forested topography. Nevertheless, retrieving snow states and properties from passive microwave sensors has long been handicapped by coarse spatial resolution (e.g., 25 × 25 km^2 of the Advanced Microwave Scanning Radiometer - Earth Observing System, AMSR-E) that cannot capture the spatial heterogeneity of the snowpack resulting in substantial random and systematic errors in complex topography and in the presence of heterogeneous vegetation, in particular forests that emit more microwave radiation than snow [19-21]. Increased absorption and decreased volume scattering in wet snowpacks (> 0.1% snow wetness), and especially in the top layers, result in loss of sensitivity with nonlinear interactions among absorption, surface scattering, and volume scattering [22,23]. Even in barren flat terrain, thermodynamically driven snow microphysics strongly affect brightness temperatures due to high sensitivity to the size of dry snow crystals that vary with time and snowpack history, and thus snowpack stratigraphy [24,25]. Wet snowpacks are especially challenging as increases in liquid water content exhibit ambiguous (i.e., noisy) brightness temperature behavior in the warm season after the onset of snowmelt processes. Recent high spatial resolution (10's m) radar backscatter measurements at intermediate wavelengths (e.g., Sentinel-1 C-Band) show little sensitivity to dry snow accumulation, and high sensitivity to surface roughness and snow surface microphysics, the interpretation of which can be further complicated by successive cycles of daytime melt and nocturnal refreeze [9], and weather variations including the spatial organization of diurnal circulations [26].

Snow hydrology models driven by near-surface atmospheric forcing provide an alternative to estimate snowpack mass and condition through accumulation and melt processes, although there is uncertainty associated with these states because of imperfect model physics and numerical approximations [24], uncertainties in meteorological forcing, land-cover and surface heterogeneities, and initial and

boundary conditions that can significantly impact model behavior [27]. Furthermore, the representation of spatial variability tied to topography, wind redistribution, and land-cover among other drivers of snowpack heterogeneity often depend on model resolution as well, and thus are tied to scale [28]. These uncertainties can be addressed in part via data assimilation of remote-sensing observations to guide model physics by constraining model states that effectively amounts to physically-based retrieval [25,29-33]. Operational (i.e., systematic, uncalibrated) robust data-assimilation requires realistic characterization of independent and correlated errors in the coupled snow-hydrology and radiative transfer dynamics as well as in the observations that are not known typically although they can be learned for the case of systematic stationary errors. Ultimately, robust data-assimilation would highly benefit from additional ground-observations for areal cross-validation (e.g., runoff) or to further constrain the model locally (e.g., snow depth) but these generally are not available in the remote and inhospitable regions of the world where snow remote sensing is needed. An alternative approach is to map the uncertainty space of snowpack physics toward determining the error bounds associated with snowpack hydrological response to variable weather and land-cover (e.g., [34]).

The objective of this paper is to develop a quantitative understanding of uncertainty propagation from spatial uncertainty in meteorological forcing of high-elevation snowpack physics to radiometric and scattering behavior. Ultimately, the goal is to separate uncertainty in snowpack microwave measurements from space (backscattering coefficient and brightness temperatures) from retrieval ambiguity tied to the spatial variability of snowpack condition. For this purpose, we rely on a multilayer snow hydrology model (hereafter referred to as MSHM) [20,21], driven by atmospheric reanalysis, and coupled to the microwave emission model of layered snowpacks (MEMLS) [35,36]. The region of study (Grand Mesa, Colorado) and available data sets are described in Section 2. The architecture of the coupled snow physics-radiative transfer modeling framework (hereafter referred to as MSHM/MEMLS) and the experimental design are summarized in Section 3. Detailed model formulations for both MSHM and MEMLS are provided in Appendices A and B, respectively. Results are presented and discussed in Section 4 focusing on seasonal snowpack hydrology (Section 4.1) and microwave behavior (Section 4.2). Synthesis and conclusions are presented in Section 5.

2. Study Area and Datasets

2.1 Study Area

The region of study is Grand Mesa (39°N ~ 39.1°N, 108.2°W ~ 107.8°W) the largest flat-top high mountain in the world (Figure 1). This is one of NASA's Snow Experiment (SnowEx) primary field sites [33], where multi-year seasonal intense field measurements are ongoing. We rely specifically on data collected during the February 2017 field campaign, hereafter referred to as SnowEx'17. Land-use land-cover (LULC) is highly heterogeneous with over 300 small lakes and ponds, evergreen and deciduous forests, grasslands and some barren soil and rock outcrops (Figure 2). Model simulations are conducted in the central part of the Mesa where most SnowEx'17 snowpit measurements were conducted.

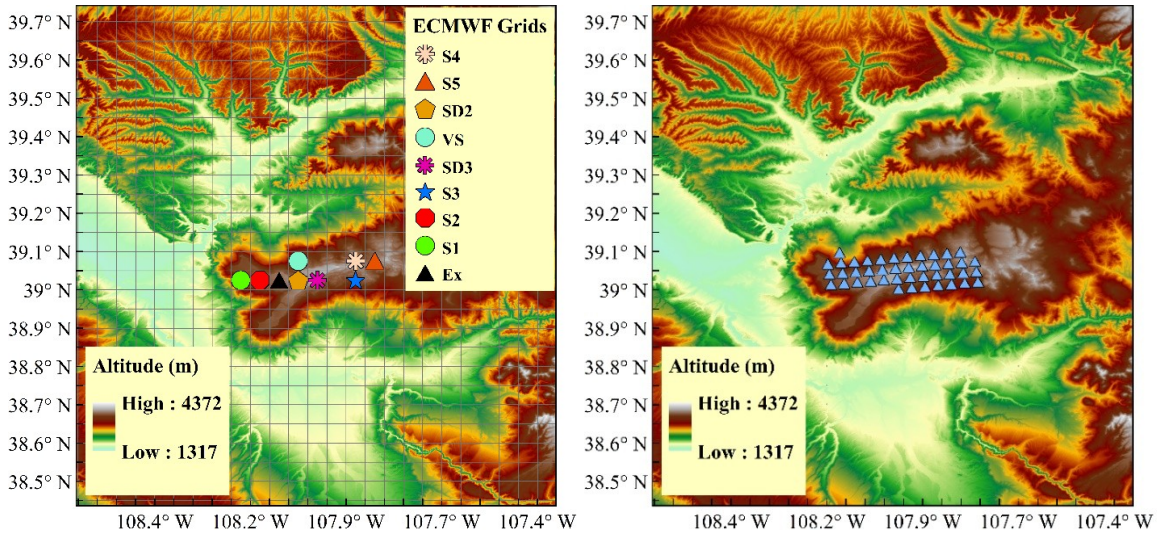

Figure 1. Topographic map of Grand Mesa with ECMWF grid cells (overlain grid on the left panel) and 43 grid points from the HRRR model (triangles on the right panel). Snowpit locations from the SnowEx'17 field campaign are clustered into 9 groups corresponding to individual ECMWF grid cells (~ 5 × 5 km^2) marked on the left panel. Each cluster contains at least eight snowpits. Table S1 in Supplementary Information provides the central (latitude, longitude) coordinates for each grid, as well as the coordinates of the HRRR grids fully or partially within the corresponding ECMWF grid. ECMWF- European center for Medium Range Weather Forecasts. HRRR- High Resolution Rapid Refresh NOAA model.

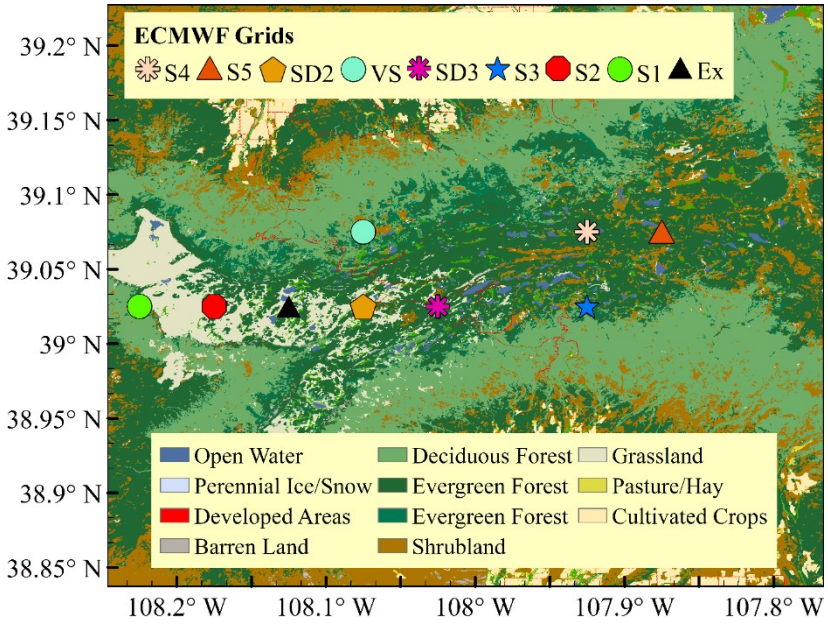

Figure 2. Land-use and land-cover (LULC) map centered over Grand Mesa. The nine snowpit clusters (Table S1) corresponding to nine ECMWF grid cells marked in Figure 1 are also marked here using the naming convention indicated in the legend.

2.2 Atmospheric Forcing

2.2.1 European Center for Medium Range Weather Forecasts (ECMWF)

Meteorological forcing (air temperature, specific humidity, wind speed, rainfall rate, snowfall rate, incoming shortwave radiation, incoming longwave radiation,

and surface albedo) utilized to drive the MSHM were obtained from the ECMWF 3-hourly reanalysis data (in UTC) with the equidistant cylindrical projection of 941 × 2336 points covering North America with (0.05° × 0.05°) spatial resolution (Figure 1, left panel). The original 3-hourly forcing was linearly interpolated to half-hourly time-steps September 1st, 2016 and June 30th, 2017, and are available at https:// barros-group.cee.duke.edu/data-access.

2.2.2 High Resolution Rapid Refresh (HRRR)

The Rapid Refresh (RAP) is a version of the Weather Research and Forecasting (WRF) model developed by the NOAA Earth System Research Laboratory (ESRL) Global Systems Division (GSD). This is an hourly updating, cloud-resolving, convection-allowing model run operationally by the National Centers for Environmental Prediction's Environmental Modeling Center (EMC) with a nominal resolution of 13 km [37]. The model domain covers the entire North America with up to 21 forecast lead times. In the spring of 2016, a high-resolution nested version of the RAP called the High Resolution Rapid Refresh (HRRR) was developed with 3-km horizontal grid and one hour update and can forecast meteorological variables up to 18 hour including: air temperature, specific humidity, wind speed, air pressure, rainfall rate, snowfall rate, incoming shortwave radiation, and incoming longwave radiation. Hourly HRRR data (data assimilation and forecast modeling systems), specifically +01 hour forecasts, used here are obtained from the Center for High Performance Computing (CHPC) at the University of Utah [38]. Time-series of HRRR meteorological data from 43 grids over the Grand Mesa (Figure 1, right panel) were linearly interpolated to the MSHM time-step (30 min) from 2016 September 1st to 2017 June 30th. Numbering and naming conventions and geographical correspondence between ECMWF and HRRR grids is provided in Supplementary Information, specifically Table S1 and Figures S1 a-b.

2.3 North American Land Data Assimilation System (NLDAS)

Initial preprocessing showed that the time-varying ECMWF albedo values are inconsistent with observed snow cover conditions over Grand Mesa and independent MODIS estimates. Surface albedo at 0.125° × 0.125° resolution (~ 12.5 × 12.5 km^2) from the North American Land Data Assimilation System (NLDAS) [39] was used instead due to its improved depiction of the diurnal variation. The average of the four NLDAS grids in the study domain was calculated first for the hourly values and subsequently interpolated to half-hourly intervals; the same value is specified for all ECMWF and HRRR grids at each time-step (i.e., the spatial variability of snow albedo across the Grand Mesa is neglected).

2.4 SnowEx'17 Field Campaign Data

Data from the NASA SnowEx campaigns can be obtained from (https://nsidc.org/data/snowex). Data relevant for this study include snow depth, SWE, snow density and temperature profiles [40]. These data are used to evaluate co-located MSHM simulations and to characterize the uncertainty associated with sub-grid heterogeneity within ECMWF grid cells and across the Grand Mesa.

Snowpit observations were obtained by digging trenches (destructive and irreversible measurements) for a one-time only sampling of the density and temperature profiles, and thus there are no repeats at the same location. It is important to highlight the gap in spatio-temporal scales between the in-situ snowpit data (point scale, near-instantaneous) and the ECMWF and HRRR forcing and MSHM simulations (kms, mins-hours). Tables S2-S4 provide geospatial

coordinates of snowpit locations corresponding to ECMWF grid cells S2, SD3 and S5 (Figure 1 and Figure 2) used in this paper to assess MSHM performance.

3. Experimental Design

3.1 MSHM/MEMLS Modeling Framework

The architecture of the coupled MSHM/MEMLS framework is summarized in Figure 3. The MSHM represents the snowpack as a multilayer column (1D in the vertical, Figure 3 right panel) with layers added (by splitting individual layers) or removed (by combining individual layers) depending on precipitation and compaction rates to meet a minimum water equivalent depth criterion for each layer (0.02 ± 0.01cm). Exchanges of mass and energy at the snowpack surface and between adjacent layers in the snowpack column (1D) are simulated using centered finite-difference approximations following [41]. The formulae used to describe key model processes are summarized in Appendix A, and the flowchart that describes model structure and linkages among model physics components is depicted in Supplementary Figure S2. Additional implementation details and alternative parameterizations can be found in [20,21]. Ongoing testing and implementation of the MSHM coupled to an existing distributed hydrology model is out of the scope of the present work. Therefore, snowpack surface conditioning (surface roughness and transient morphology), snow erosion and redistribution by winds, and the structural effects of forest cover on snow hydrology on the one hand and on microwave behavior on the other are not described in the version of the MSHM/MEMLS used here. The latter are at best accounted for only in the time-varying values of albedo specified and in the atmospheric forcing (specifically, low level winds, air temperature and relative humidity) to the extent that land-cover is parameterized in the underlying numerical weather prediction model.

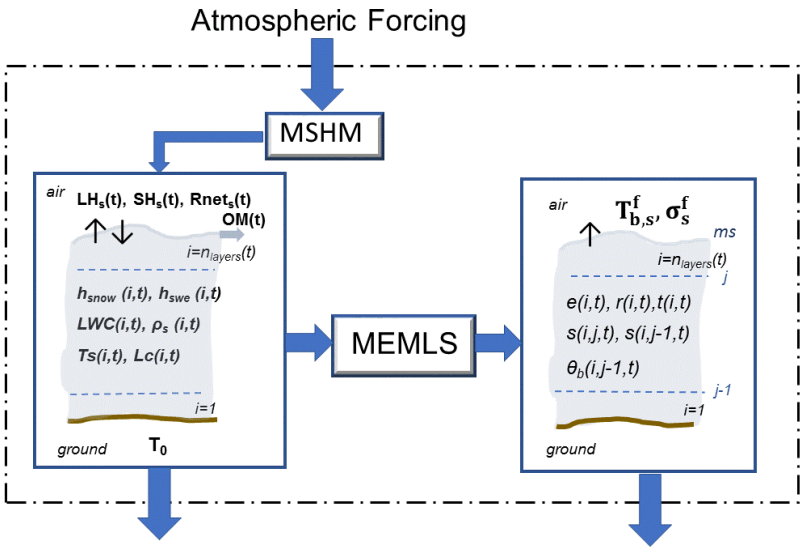

Figure 3. Information flow diagram in the coupled MSHM/MEMLS framework. At a given time t, the MSHM simulates a snowpack consisting of number of layers $n_{layers}(t)$, and yields snowpack stratigraphy consisting of the vertical profile of layer thickness (h_{snow}), snow water content (h_{swe}), liquid water content (*LWC*), density(ρ_s), temperature T_s including ground temperature T_0, and snow correlation length L_c. At the surface of the snowpack, latent heat (*LH*), sensible heat (*SH*), net radiation (*Rnet*), and outmelt (*OM*) fluxes are also calculated. The snowpack stratigraphy and temperature profiles are passed onto MEMLS to simulate the vertical profiles of transmissivity t, volume reflectivity *r*, emissivity *e*, interface reflectivity *s*, and refracted angle θ_b where j=i. Incoming

electromagnetic radiation (not shown) hits the snowpack surface of roughness *ms* with incidence angle θ_n (not shown). The MEMLS output is brightness temperature $T_{b/s}$ and backscattering coefficient σ_s at the surface for frequency f, horizontal and vertical polarization.

The MEMLS model was developed based on six-flux theory to simulate multiple volume scattering and absorption (Figure 3, right panel) including radiation trapping from internal and coherent reflections at layer interfaces (see Figures S3 and S4). It was first implemented to simulate multi-frequency microwave brightness temperatures [36] with good performance compared to satellite data [20,21], and it has been further enhanced to simulate backscattering [35]. Implicit in the MSHM/MSML coupling is the common spatial scale determined here by the spatial scale of the atmospheric forcing, and the assumption that there is no subgrid-scale variability in snowpack states (e.g., snow types) that would introduce variability in the microwave emissions and backscatter [23,26]. The coupled MSHM/MEMLS modeling framework is run continuously in fully predictive mode from September (9/1/2016) through June (6/30/2017) at half-hourly time-steps driven by independent meteorological forcing (ECMWF, HRRR). SnowEx'17 snowpit measurements during February 2017 are used for evaluating MSHM predictability of snowpack physical properties and snow hydrologic states. The density of fresh snow is specified as 30 kg/m^3.

3.2 Ensemble Design

The impact of uncertainty tied to the spatial variability of meteorological forcing on the simulated snowpack's physics and microwave behavior is investigated using ensemble forecasts (EF). Two ensemble families were designed. Members of the first ensemble family (EFF1, 3 km resolution) are obtained by replacing ECMWF forcing with HRRR "perturbations" neglecting spatial resolution differences between ECMWF and HRRR. EFF1 consists of 6 different ensembles (0-5) each corresponding to different combinations of ECMWF and HRRR forcing as summarized in Table 1 for a total of 2,322 simulations (9 ECMWF grids × 43 HRRR perturbations = 387 members for each of the 6 EFF1 ensembles). Members of the second ensemble family (EFF2, 750 m resolution) are obtained by replacing HRRR precipitation analysis at the native 3km resolution with 16 precipitation replicates obtained by fractal downscaling of the HRRR precipitation fields [42-45]. For reference, the cumulative snowfall and rainfall curves and the concurrent time-series of near-surface air temperature (2 m) from the HRRR analysis are provided in Figure S5. EFF2 consists of 9 ensembles for each of the HRRR grids nearest to the centers of nine ECMWF reference grids with 16 members for a total of 144 simulations. Figure S6 illustrates graphically the downscaling strategy. Note that the fractally downscaled precipitation at 750 m resolution is itself the ensemble mean of fifty rainfall fields generated recursively [43,45]. Whereas it is possible to downscale the precipitation to higher spatial resolution, recent work [9] suggests that there is robust interpretable scaling behavior in SAR measurements at C- and L-bands at spatial scales in the 400-1,000 m range.

Table 1. Summary description of Ensemble Forecast Family 1 (EFF1) design. Grand Mesa ensembles are produced using 9 ECMWF and 43 HRRR distinct forcing time-series. Data are available at https://barros-group.cee.duke.edu/data-access.

Ensemble	**0**	**1**	**2**	**3**	**4**	**5**
Air temperature (K)	ECMWF	HRRR	HRRR	HRRR	HRRR	HRRR
Snowfall rate (kg/m2/s)	ECMWF	ECMWF	HRRR	HRRR	HRRR	HRRR
Rainfall rate (kg/m2/s)	ECMWF	ECMWF	HRRR	HRRR	HRRR	HRRR

Air pressure (Pa)	HRRR	HRRR	HRRR	HRRR	HRRR	HRRR
Incoming shortwave radiation (W/m2)	ECMWF	ECMWF	ECMWF	ECMWF	ECMWF	HRRR
Incoming longwave radiation (W/m2)	ECMWF	ECMWF	ECMWF	ECMWF	ECMWF	HRRR
Albedo	NLDAS	NLDAS	NLDAS	NLDAS	NLDAS	NLDAS
Windspeed (m/s)	ECMWF	ECMWF	ECMWF	HRRR	HRRR	HRRR
Specific humidity (kg/kg)	ECMWF	ECMWF	ECMWF	ECMWF	HRRR	HRRR
Ensemble Size	387	387	387	387	387	43

The EFF1 ensemble spread is tied to the forcing uncertainty at 3 km resolution over the relatively large Grand Mesa domain (Figure 1), whereas ensemble differences among each of the nine ECMWF reference grids reflect differences in land-cover and land-form that impact surface roughness, and thus friction velocity and surface winds. The EFF2 ensemble spread stems from increased spatial variability of precipitation from 3 km (HRRR pixel) to 750 m (downscaled precipitation), and aims to capture the uncertainty tied to the stochastic redistribution of precipitation at HRRR sub-grid scales.

4. Results and Discussion

To characterize uncertainty in snowpack microwave behavior (backscattering coefficient and brightness temperatures) tied to snowpack states conditional on regional weather, we view the coupled snow hydrology-radiative transfer model as an instrument simulator. A key challenge therefore is that the snow hydrology model must represent the governing physical processes and capture the fundamental drivers of radiative properties changes in the snowpack. Thus, we start by evaluating the model's capability to capture snow hydrologic processes and quantifying the range of uncertainty in snowpack hydrologic properties associated with meteorological forcing in Section 4.1. The active and passive microwave behavior of the snowpack is examined in Section 4.2. Analysis of model results and discussion is centered on ECMWF grid cells S2, SD3, and S5 (Figure 1) to capture the evolution of the snowpack in the western, central, and eastern sub-regions of Grand Mesa, respectively. Each of these three grids is collocated with HRRR grids and contains several snowpit observations obtained during SnowEx'17 (snowpit geo-coordinates and acquisition dates and times are provided in Tables S2-S4).

4.1 Snowpack Hydrology

SWE and Snow Depth – SWE and snow depth predictions begin on 9/1/2016 and last till 6/30/2017 for each EFF1 ensemble to capture the full seasonal evolution of the snowpack in Grand Mesa as shown in Figure 4. The severe snowfall underestimation in the ECMWF forcing is apparent in the Ensemble 0 and Ensemble 1 results amounting respectively to 100% and 300% difference with regard to Ensemble 2 and Ensemble 5 SWE and snow depth. The contrast in spread of the yellow (25^{th} and 75^{th} percentiles) and green (max and min) envelopes between Ensembles 0 and 1 demonstrates the impact of the space-time variability of near-surface air temperature in driving heterogeneity among ensemble members. Solid and liquid precipitation are not specifically differentiated, and standard approaches, such as using near-surface air temperature below a certain threshold (e.g., 273.15 K) to identify snowfall, do not work well because the ECMWF near-surface air temperature exhibits strong warm bias as compared to observations and to HRRR values as well. Indeed, excessive early warming leads to the dramatic melting and snowpack retirement almost two weeks earlier in Ensemble 1. Dramatic improvement is achieved when the HRRR precipitation

forcing is introduced in Ensemble 2. There are no significant differences in snow mass accumulation and melt patterns among Ensembles 3 and 4 (not shown) and Ensemble 5, indicating that precipitation and air temperature, and in particular snowfall, are the key local meteorological forcing necessary to capture the seasonal snowpack over Grand Mesa as long as radiative forcing and winds are representative of regional conditions. This result is expected and consistent with [27] who found that sensitivity of a snow hydrology model to forcing was dominated by precipitation bias errors.

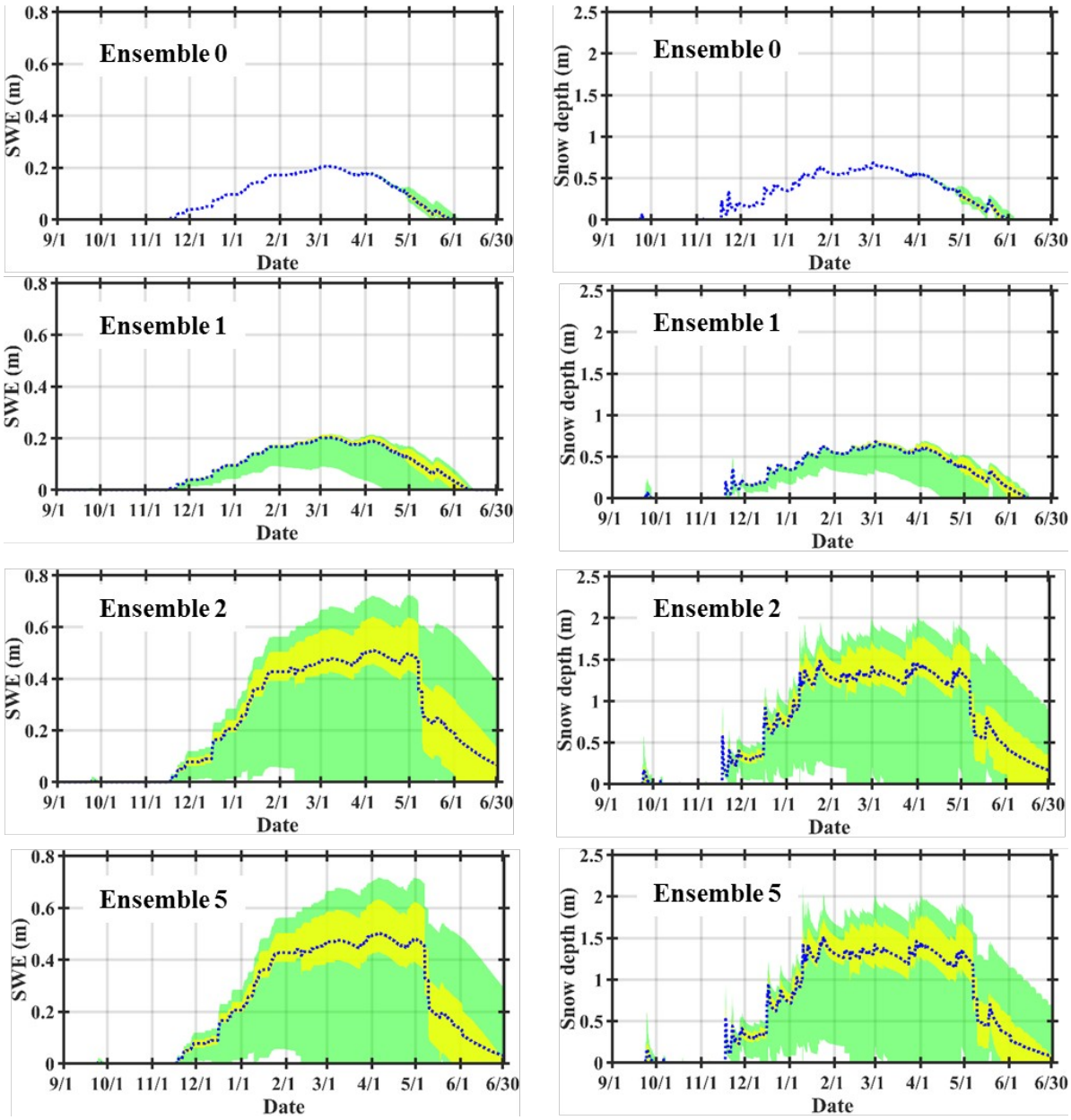

Figure 4. Time series of ensemble SWE predictions from 9/1/2016 through 6/30/2017 (left panels) and snow depth (right panels) for Ensemble 0, 1, 2 and 5 (Table 1) from top to bottom respectively. The blue dotted line is the ensemble mean. The green envelope identifies the ensemble range, and the yellow envelope delimits the 25th and 75th percentiles.

Figure 5 compares SnowEx'17 snowpit measurements at S2, SD3 and S5 and MSHM Ensemble 5 evolution of SWE (left panels) and snow depth (right panels). For reference, the cumulative predicted snow mass (SWE) in February 2017 at the ECMWF grid cell scale (~ 5 × 5 km^2) does not reach the highest measured value

across the Grand Mesa, which can be attributed in part to HRRR underestimation of precipitation generally, and snowfall in particular, uncertainty in the snowpit measurements themselves, as well as uncertainty due to the scale gap between point measurements (the individual snowpits) and Ensemble 5 members that represent areal averages at the HRRR grid cell scale (3 × 3 km^2). One additional source of snow depth uncertainty is the empirical parameterization of snowpack compaction in the model (Appendix A, Section A.1). Specifically, the terms corresponding to overburden effects exhibit high sensitivity to snow accumulation, and therefore propagate nonlinearly the uncertainty in snowfall to snow depth.

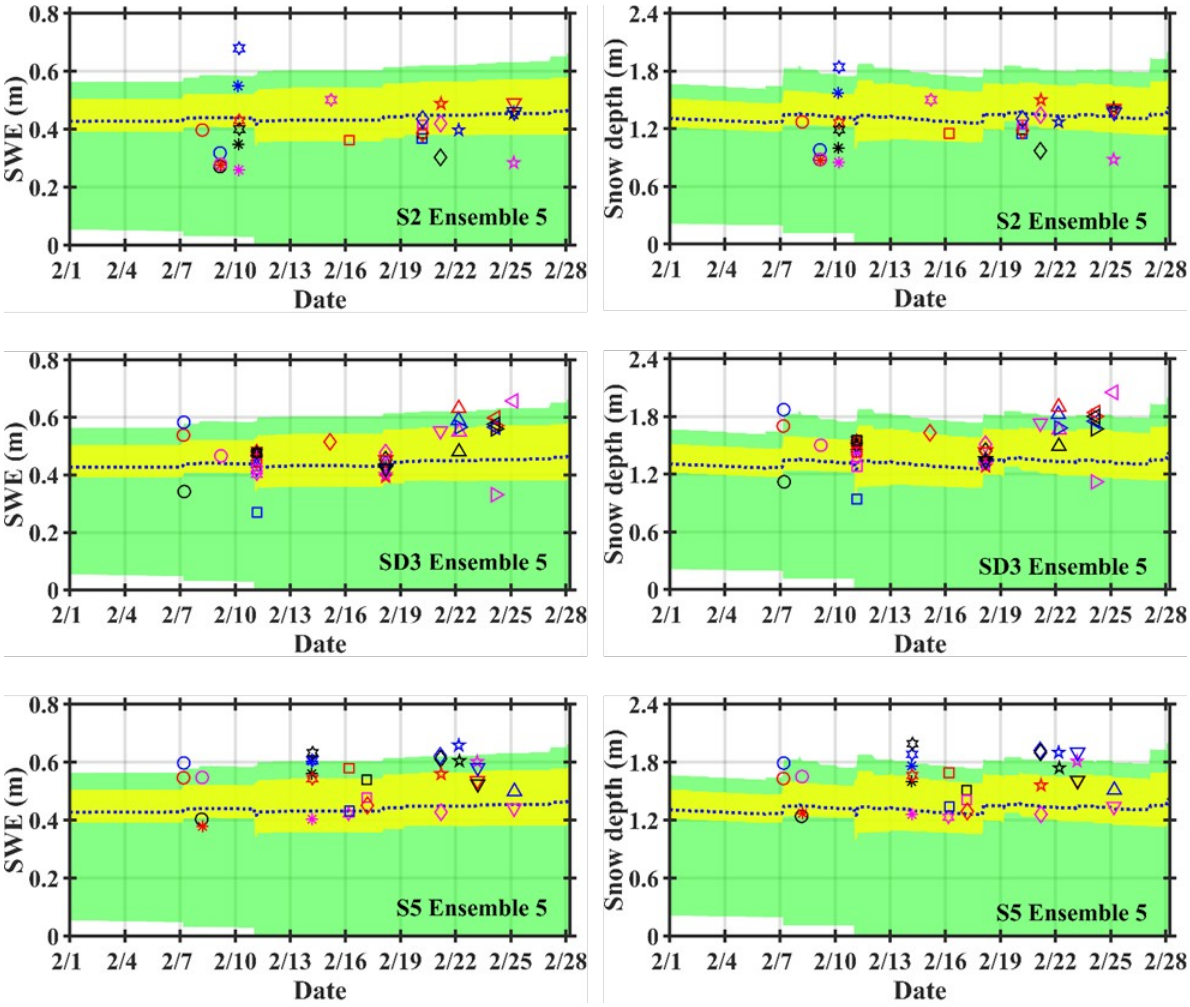

Figure 5. Time series of Ensemble 5 SWE (left column) and snow depth (right column) predictions on February 17 at S2 (top row), SD3 (middle row) and S5 (bottom row). The blue dotted line is the Ensemble 5 mean. The green envelope identifies the minimum and the maximum values among all ensemble members, and the yellow envelope delimits the 25th and 75th percentiles. The symbols represent the SnowEx'17 snowpit observations following the convention in Table S2.

The model results during SnowEx'17 were organized further in two sets for evaluation against the snowpit measurements according to spatial scale: a) local – Ensemble 5 predictions for the member that is nearest to the center of each reference ECMWF grid (Table S1), and b) global – Ensemble 5 mean across the Grand Mesa. Figure 6 shows the local (top row) and global (bottom row) model bias during February 2017. Inspection of the local bias (local Ensemble 5 member – snowpit average within the corresponding ECMWF grid cell) shows that SWE estimates are within ±10% of the snowpit measurements except at S1 and S5. This indicates that the HRRR snowfall estimates and the model handling of the

snowpack mass and energy budgets are well simulated without the need for calibration or special processing of the data. The large accumulation biases at S1 (positive bias, surplus) and S5 (negative bias, deficit) are attributed to uncertainty in wind effects. Sources of uncertainty in near-surface wind magnitudes include the fact that HRRR near-surface winds are used directly in the simulations without downscaling which introduces large biases in the surface friction velocity everywhere [46], lack of topographic corrections to account for the steep slopes at S1 in the western edge of the Mesa, and corrections to account for structured roughness due to the presence of forest at S5. Additionally, as mentioned earlier, the MSHM implementation used here does not simulate wind-redistribution. This explanation is further supported by the temporal variability of the global bias (Ensemble 5 mean – snowpit average within the reference ECMWF grid cell) as well as the west-east differences with larger negative bias to the east (e.g., SD2, SD3 and S5) on the more forested areas of the Grand Mesa as snow accumulates in the second half of February (see Figure 2) and larger positive bias to the west (e.g., S1).

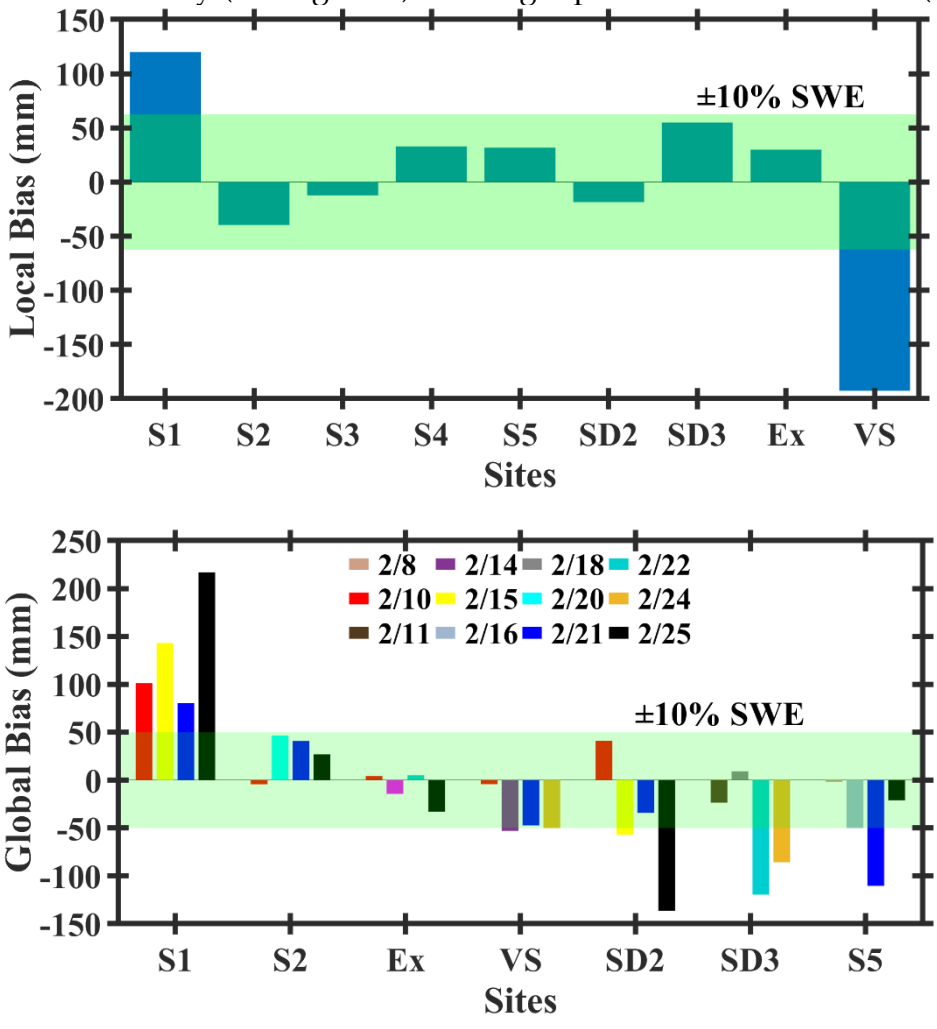

Figure 6. Evaluation of model bias at reference ECMWF grid points (Figure 1) during SnowEx'17 (Table S1). **Top** – Local bias calculated as the difference between the Ensemble 5 Member corresponding to the nearest HRRR grid and the average of SnowEx'17 snowpit measurements within each ECMWF reference grid point for the entire month of February. **Bottom** – Temporal evolution of global bias calculated as the difference between the Grand Mesa Ensemble 5 mean and the average snowpit measurements on the same day within each ECMWF reference grid point.

Snow Stratigraphy – The temporal evolution of snow density and temperature profiles at S2 corresponding to Member 8 of Ensembles 1, 2 and 5 are shown in

Figure 7. The average of co-located snowpit profiles is superimposed on simulated profiles for the available dates. As expected Ensemble 5 members are the most realistic in that the simulated snow depths are close to the measurements. There is however no significant difference in the temperature gradients in the upper half of the simulated snowpack among members of Ensembles 2 and 5, demonstrating the governing role of the near-surface air temperature in the turbulent heat exchange at the air-snow interface. The differences between model and snowpit average density are generally less than 50 kg/m^3 at the same depth, which is adequate for coupled forward modeling of snow hydrology and radiative transfer using MEMLS [20-22,34].

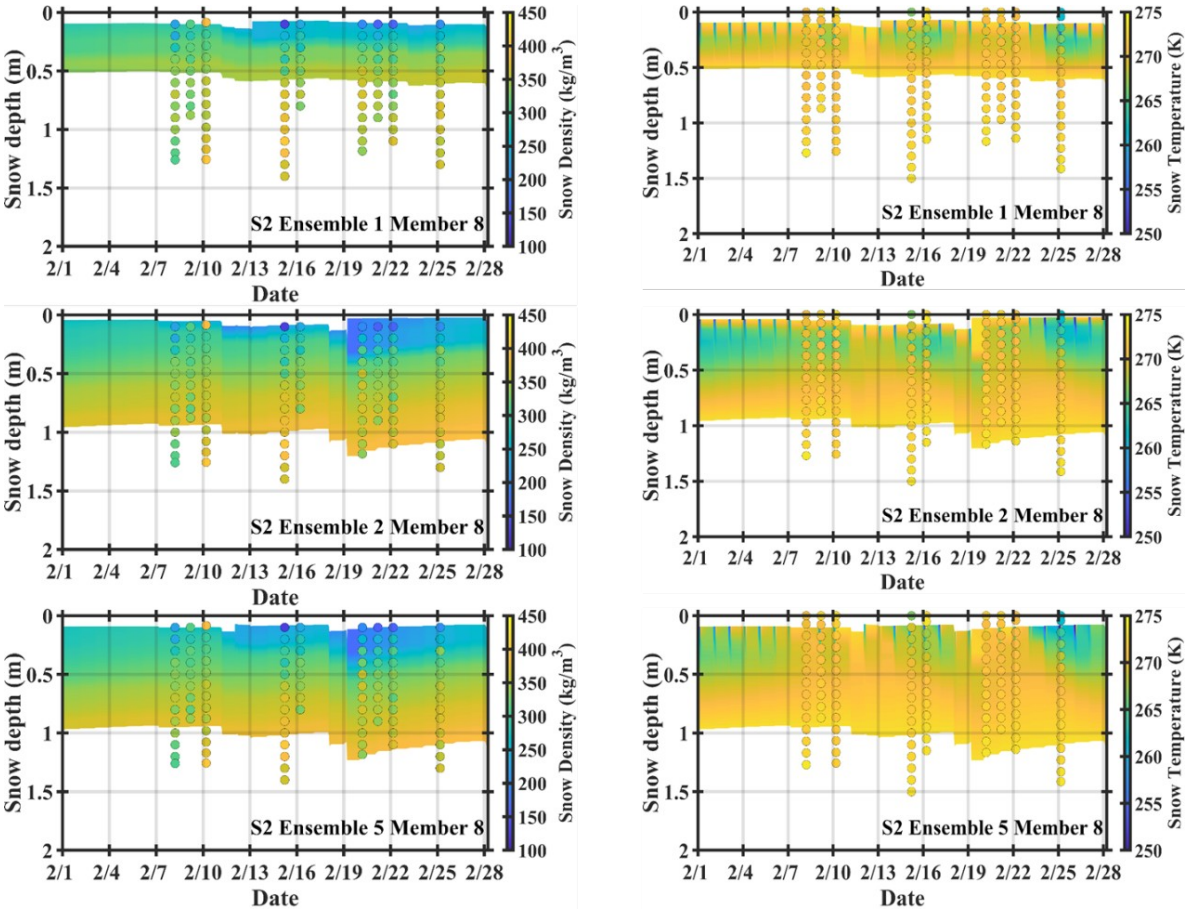

Figure 7. Evaluation of predicted snow density and temperature profiles at S2 by Member 8 (HRRR grid point closest to the center of the S2 ECMWF grid point, Figure S1a) for Ensembles 1, 2 and 5 in the top, middle and bottom rows respectively. The circles represent the average of snowpit density (left column, color scale on the right) and temperature (right column, color scale on the right) measurements as a function of depth (on the left-hand side y-axis) and date (x-axis). The measured values are plotted at the depth of measurement in the SnowEx'17 records. The model values are plotted at the mid-point of each layer. Time-series of simulated snowpack stratigraphy (number of layers and layer thickness) are provided in Supplementary information (Figure S7a).

Temperature and density profiles at SD3 (Member 13) and S5 (Member 29) for Ensemble 5 only are shown in Figure 8. Ensemble 5 model predictions capture well the isothermal behavior of the snowpack at the three sites (bottom row in Figure 7 for S2, and Figure 8 for SD3 and S5) as well as the signature of major snowfall and cold weather events. The temporal evolutions of the number of snowpack layers and top layer depth simulated for the three reference grids are shown in Figure S7. SnowEx'17 measurements of top-layer snow temperatures are generally close to the freezing point (273.15 K) and nearly isothermal throughout the snowpack

except during two cold periods on February 15 and February 25. Daytime temperatures well below the freezing level in the top 20-50 cm for these two events that are well captured by the model consistent with the local surface energy budget. For instance, Figure S8 shows the strong reduction in daytime snowpack sensible heat flux at S2 in the February 22-25 period. In addition, note the short-lived periods of steep decreases in upper snowpack temperature tied to transient decreases in cloudiness that translate into approximately halving of incoming longwave radiation in the February 22-25 period (e.g., Figure S9). The contribution of incoming longwave radiation to the surface energy budget is critical [47], and the reduction of incoming longwave radiation (~ 150 W/m^2) on clear cold days impacts snowpack temperatures at intermediate depths corresponding to the top 50 cm at S2 and as much ~100 cm for the deeper snowpack at SD3 and S5 (Figure 8) due to faster cooling in less dense snow.

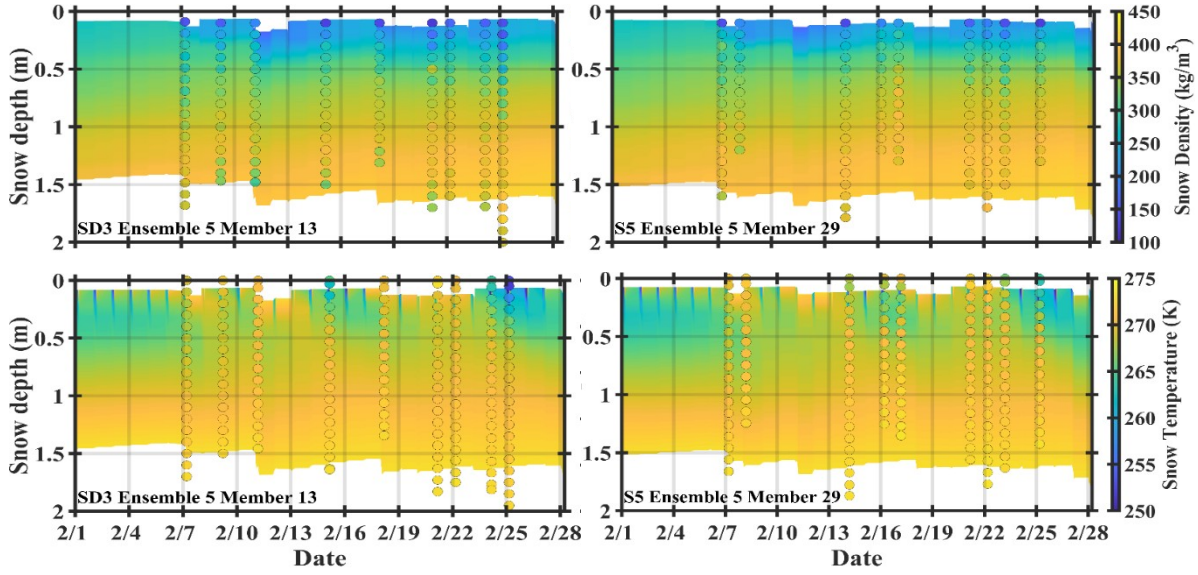

Figure 8. Evaluation of predicted snow density (top row) and temperature (bottom row) profiles against measured snowpit profiles (circles). Left column: Ensemble 5 Member 13 (HRRR grid point closest to the center of the SD3 ECMWF grid, Figure S1a). Right column: Ensemble 5 Member 29 (HRRR grid point closest to the center of the S5 ECMWF grid, Figure S1a). The measured values are plotted at the depth of measurement in the SnowEx'17 records. The model values are plotted at the mid-point of each layer. Time-series of simulated snowpack stratigraphy (number of layers and layer thickness) are provided in Supplementary Information (Figures S7b and S7c).

Figure 9 illustrates the behavior of Ensemble 5 against measurements from each of four snowpits within S2 on February 25. A caveat of daytime snowpit profile measurements is that they are disturbed at least in part due to excavation and the snowpack facies is directly exposed to the environmental air, which can explain at least in part the warmer temperatures in the deeper layers. The goal here is to compare the ensemble spread with the snowpit measurements' spread within S2, where the ensemble spread captures snowpack heterogeneity tied to the space-time variability of meteorological forcing within the Grand Mesa at the small mesoscales of the HRRR analysis (3 × 3 km^2), and the snowpit measurements represent subgrid-scale variability. Simulated snow density profiles replicate closely the measurements except at the bottom of the snowpack where the measured density profiles display an "inversion" with lower densities 5-20 cm above the snow-soil interface (e.g., top right in Figure 9). This behavior suggests depth hoar formation at the snow-soil interface that is not explicitly represented in the model.

Overall, the MSHM driven by HRRR atmospheric forcing and constrained by the mass and energy balance exhibits behavior consistent with SnowEx'17 snowpit observations across the Grand Mesa. Figure 10 shows the continuous simulation of snowpack temperature, density and snow correlation length profiles for the 2016-2017 hydrologic year including accumulation and melt regimes. The decreases in density and cold temperatures at the top of the snowpack during and after snowfall are depicted well by the model, including the densification of the uppermost layers, the nearly isothermal profiles during warm periods that result from surface melt retained in the top layer or can percolate and freeze as shown in Figure 7. Note the long duration of the snow-on season in 2017 that lasts till the end of June consistent with Landsat and Sentinel-1 satellite observations [9].

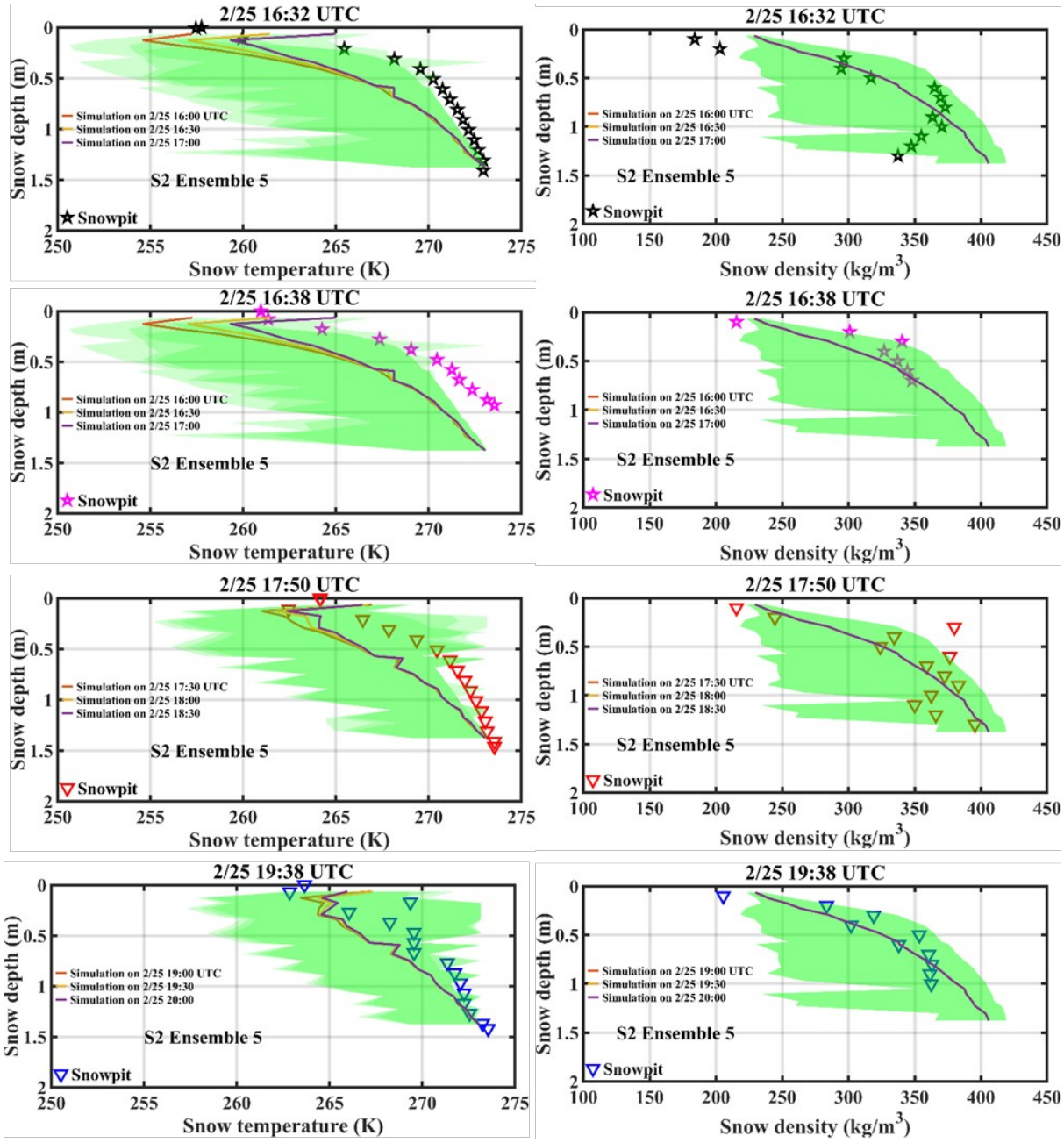

Figure 9. Evaluation of Ensemble 5 predictions of snow temperature (right) and snow density (left) against snowpit measurements within S2 on February 25. The continuous lines represent Ensemble 5 mean values at three distinct times close to the reported time of snowpit measurements. The green envelope represents the min-max range of ensemble predictions at each depth. Each row is

associated with one of four distinct snowpits identified by distinct markers according to the convention in Table S2.

A side-by-side survey of Figure S5 (meteorological forcing: precipitation and air temperature), Figure 4 (bottom row, snowpack SWE and snow depth), and Figure 10 (snowpack stratigraphy) shows modest uncertainty in SWE (~ ±15%) and snow depth (~ ±10%) during the accumulation regime tied to snowfall uncertainty that is maximum in the winter. At the Grand Mesa scale, uncertainty peaks in the melting season with values up to 50% attributed to weather, and in particular air temperature. Interestingly, uncertainty in snow density as a function of snow depth (mid panel in Figure 10) is significantly larger in the fall season and through the warming period in the first half of February (top panel in Figure 10). It collapses as the snowpack ages and becomes deeper during the accumulation season, and large variations in density with fresh snowfall are limited to the top 50 cm. The layering in the vertical structure of snow correlation length reveals the stratigraphy of snow microphysics (bottom panel in Figure 10) to be more complex than suggested by the apparent simplicity of the physical parameterization used in the model that expresses a linear dependence of snow correlation length with temperature [36,48]. This complex stratigraphy is the outcome of the temporal integration of nonlinear interactions among snow aging processes, the diurnal cycle of radiative forcing and weather systems that affect the snowpack temperature, and the occasional fresh snowfall and rain-on-snow events. Snowpack microphysical and thermodynamic stratigraphy along with snow mass and surface roughness govern the effective radiative properties of the snowpack, and its emissions and scattering behavior to be discussed next.

4.2 Snowpack Microwave Emissions and Scattering Behavior

The snowpack ensembles generated by the snow hydrology model were used to generate dual-polarization backscatter coefficients (σ) and brightness temperatures (Tb) at L- (1.3 GHz), C- (5.6 GHZ) and Ku– (13.5 GHz) and Ka- (37.5 GHz) bands using MEMLS with parameters summarized in Table 2 for both EFF1 and EFF2 ensembles. The objective is to examine the propagation of spatial uncertainty associated with meteorological forcing at the Grand Mesa scale in the microwave domain, and to estimate uncertainty due to sub-grid scale variability of precipitation, respectively. Only a selection of results that synthesizes the main findings is shown here. We quantify sensitivity in terms of ensemble standard deviation and range.

Table 2. Parameters set for active and passive microwave remote sensing of snow in MEMLS. The type of scattering coefficient refers to specific parameterization of the 6-flux scattering coefficients, and 11 was proved to be the best [35].

Frequency (GHz)	1.3, 5.6, 13.5, and 37.5 GHz
Incidence angle (°)	50
Snow-ground reflectivity, h-pol	0
Snow-ground reflectivity, v-pol	0
Specular part of snow-ground reflectivity, h-pol	0
Specular part of snow-ground reflectivity, v-pol	0
Sky brightness temperature (K)	0
Type of scattering coefficient	11
Mean slope of snow surface undulations	0.1
Cross polarization fraction	0.2
Snow salinity (parts per thousand)	0

Sensitivity to Meteorological Forcing – The propagation of uncertainty from the snow hydrology to the microwave radiative transfer model is examined first by contrasting C-band (5.6 GHz) active σ-HH and passive Tb-H and active Ka-band (37.5 GHz) for EFF1 Ensembles 2 and 5 that differ in atmospheric forcing with regard to boundary-layer conditions (wind speed and specific humidity) and incoming radiation (Table 1). Recall that there is a small net change in SWE (< 5 cm) during the month of February in Grand Mesa, and the variability on each date reflects mostly the concurrent spatial variability of snowpack radiative properties. The results (Figure 11) for Ensemble 2 exhibit much less variability than the results for Ensemble 5, which can be attributed to the latter's improved spatial variability of the boundary-layer (including winds and specific humidity, and cloudiness) that modulates the surface energy budget the independently of frequency across the Grand Mesa. Backscatter and brightness temperatures exhibit highly nonlinear sensitivity as measured by the standard deviation, respectively ±10 dB and ±2 K, and that this sensitivity is more significant in the case of active microwave at the longer wavelength (i.e., 5.6 GHz), albeit the range is nearly twice as large. Note the collapse of the violin diagrams and thus uncertainty during the cold snap in late February as well as the higher σ with larger uncertainty for Ka- compared to C-band. For the remainder of this discussion, the discussion will focus on EFF1 Ensemble 5 results.

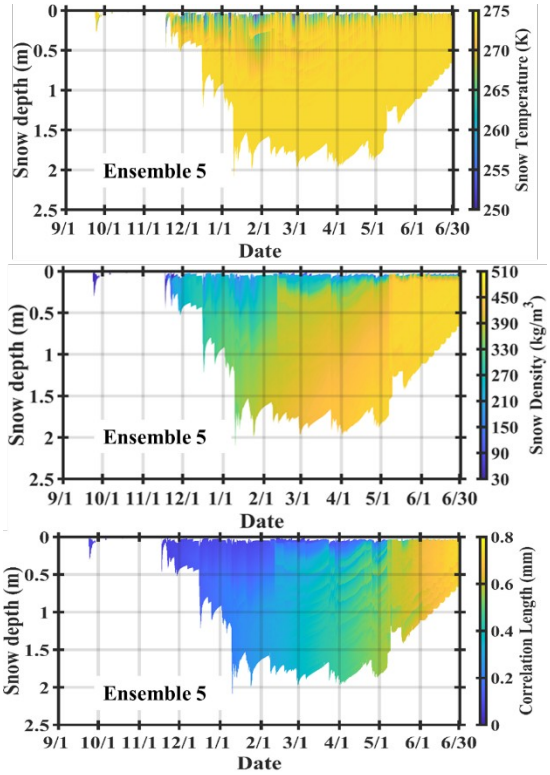

Figure 10. Ensemble 5 predictions of seasonal evolution of snowpack vertical profiles contoured by temperature (top panel), density (mid panel) and snow correlation length (bottom panel) from 9/1/2016 through 6/30/2017.

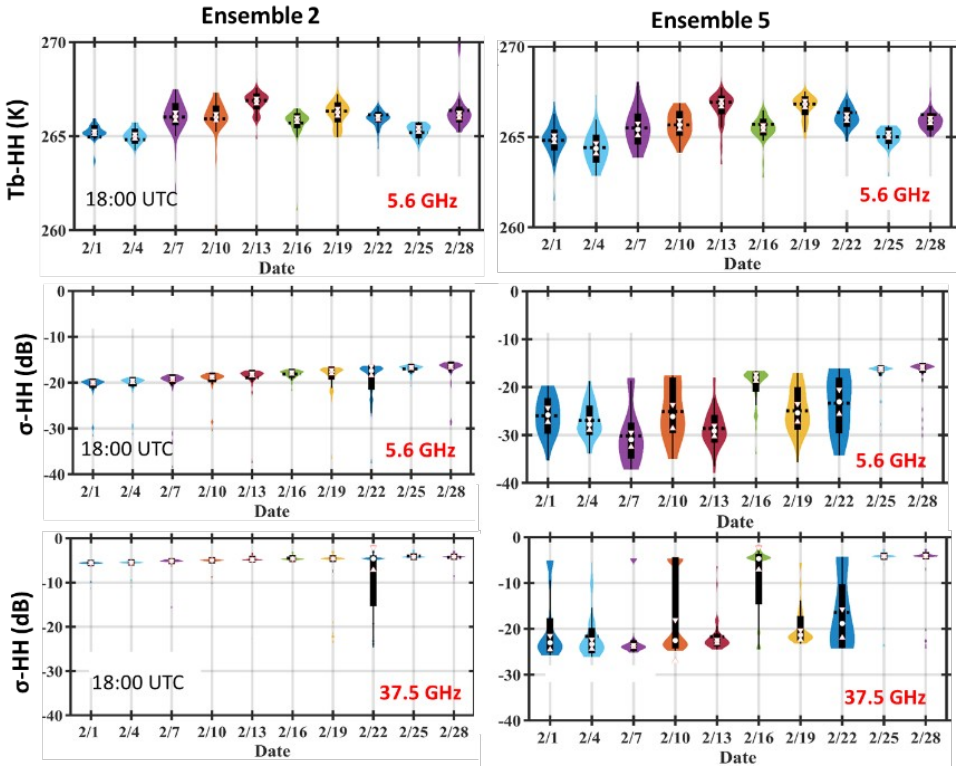

Figure 11. Spatial variability of brightness temperatures (Tb, top panels) HH-pol and backscattering coefficients for C- (5.3 GHz, mid-panels) and Ka- (37.5 GHz, bottom panels) bands at 18:00 UTC (1 PM MST) across the Grand Mesa from Ensemble 2 (left column) and Ensemble 5 (right column) during February 2017. For each violin diagram, the white dot represents the median; the horizontal black dashed line is the mean; the vertical black bar demarks the 25th and 75th percentiles; the upper and lower bounds represent the maximum and minimum values respectively; and finally, the colored contour is the density distribution.

Figure 12 shows the temporal evolution of backscattering coefficient σ HH- and σ VH-pol at 5.6 GHz and 1.3 GHz contoured by Ensemble 5 SWE during February 2017. The ensemble mean highlights the diurnal cycle of backscattering sensitivity that peaks in the afternoon when the spatial variability of HRRR radiative forcing and planetary boundary layer conditions is the highest, and when daytime warming of the snowpack peaks causing surficial melt for some ensemble members. Note the much higher sensitivity overall at 5.6 GHz including for high SWE ensemble members in the afternoon. The compound effect of standard deviation of snow depth and snowpack condition explains the large range (up to 20 dB) among ensemble members (e.g., 2/12 – 2/17, 2/19-2/22 and 2/23). The decrease in uncertainty on 2/11, 2/17 - 2/18, and in the evening of 2/22 is associated with the addition of fresh snow to the snowpack across the Mesa as shown in Figure S10. Rain-on-snow for some of the ensemble members on 2/11 and 2/17-2/18 and very warm air temperatures that cause surficial melting in the case of other ensemble members enhance nighttime sensitivity at 5.6 GHz due to the increase in liquid water content in the top layers of the snowpack (e.g., Figure 13). Further, nighttime temperatures above the freezing point for some HRRR grids explain the differences in nocturnal sensitivity of the snowpack between 5.6 GHz and 1.3 GHz in the evening of 2/10 and early morning of 2/11.

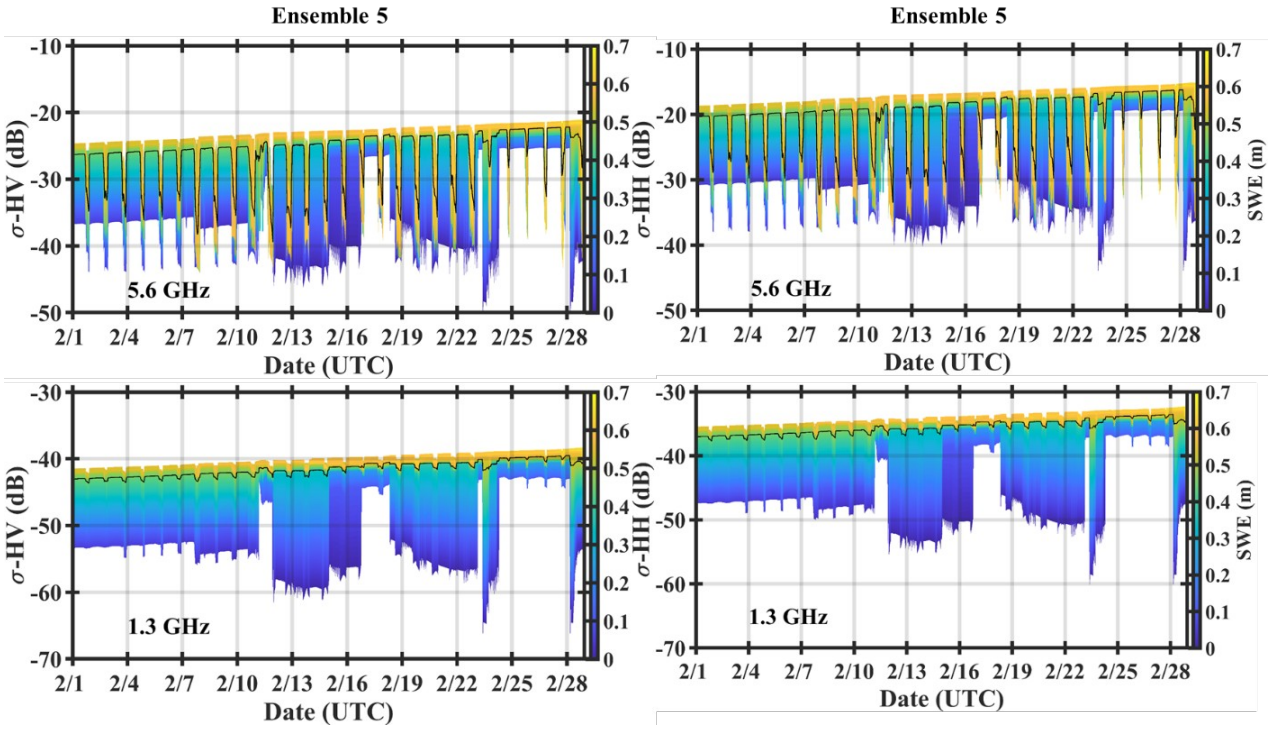

Figure 12. Temporal evolution of ensemble backscattering coefficient σ-HH and σ-HV at 5.6 GHz (top panel) and 1.3 GHz (bottom panel) contoured by Ensemble 5 SWE. The black line is the Ensemble 5 mean. Note the diurnal cycle of sensitivity of the ensemble mean that is dominant at 5.6 GHz including for high SWE ensemble members.

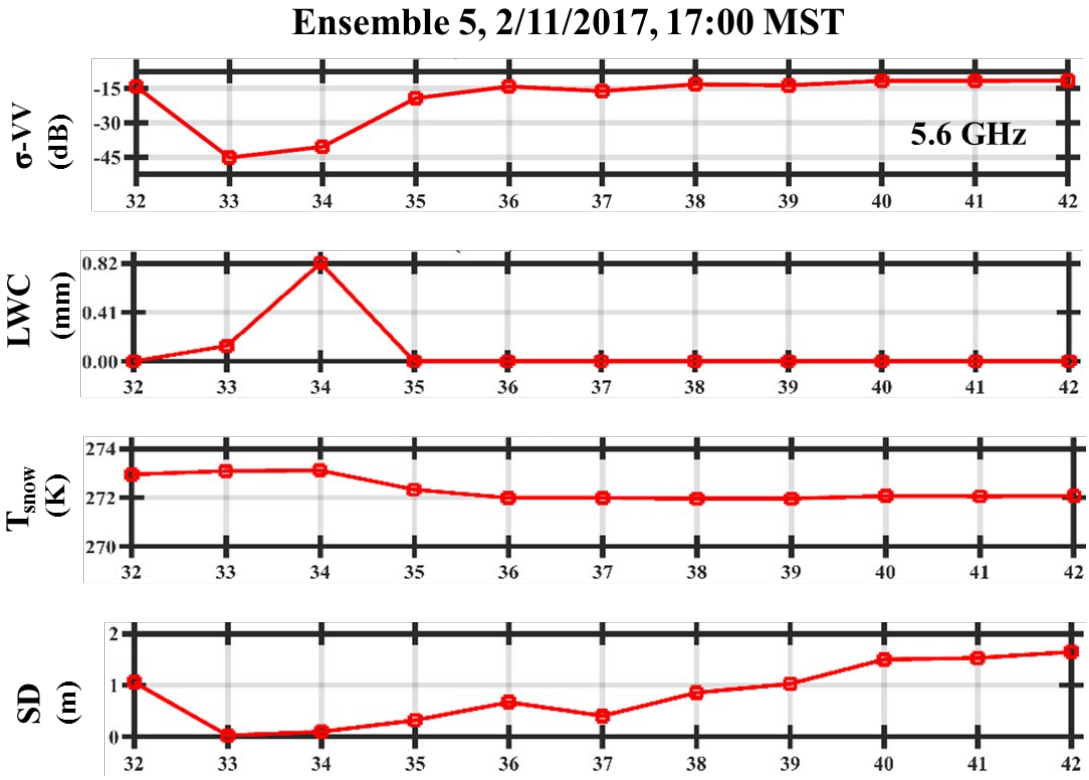

Figure 13. Backscattering behavior of σ-VV at 5.6 GHz and snowpack properties along the west-east transect formed by Ensemble 5 Members 32-42 in Grand Mesa (see maps in Figure 1 and Figure S1). LWC – liquid water content in the top snow layer. Tsnow – temperature of the top snow layer. SD – snowpack depth. MST – Mountain Standard Time = UTC-7.

582 Figure 14 shows how melting during the second week of February reduces
583 snowpack depth and SWE (Figure 12) and exposes deeper layers with longer snow
584 correlation length (red box). The signature of long correlation lengths in the top
585 snowpack layer exposed by melt in Figure 14 remains till the end of the month
586 although it becomes narrower over time as new snowfall resets the top layer snow
587 correlation length to much lower values. Nocturnal sensitivity (Figure 12 and
588 Figure 14) collapses during the severe cooling event with intermittent snowfall at
589 the end of the month (after 2/23). Daytime sensitivity peaks in the afternoon for
590 some ensemble members, and at 5.6 GHz in particular as the weather begins to
591 warm up on 2/26. The contrast between scattering behavior at 7 AM MST (similar
592 for 7 PM LST) and 2 PM MST is illustrated in Figure S11 for the month of January
593 and February in 2017. At 7 AM MST, Ensemble 5 variance that captures the spatial
594 variability attributed to meteorological forcing across the Grand Mesa at 3×3 km^2
595 remains at or below 3 dB for both 1.3 GHz and 5.6 GHz with very little difference
596 between the two except on January 9 (bottom left), when there is a very large
597 snowstorm and a significant increase in snow depth. At 2 PM MST, the standard
598 deviation does not significantly change at 1.3 GHz, but it increases up to 8 dB at 5.6
599 GHz tied to surface melt. Indeed, daytime snowmelt and subsequent nighttime
600 refreeze previously identified by [9] in Grand Mesa using Sentinel 1, C-band (5.6
601 GHz) SAR measurements is the most important source of variability in the
602 accumulation regime.

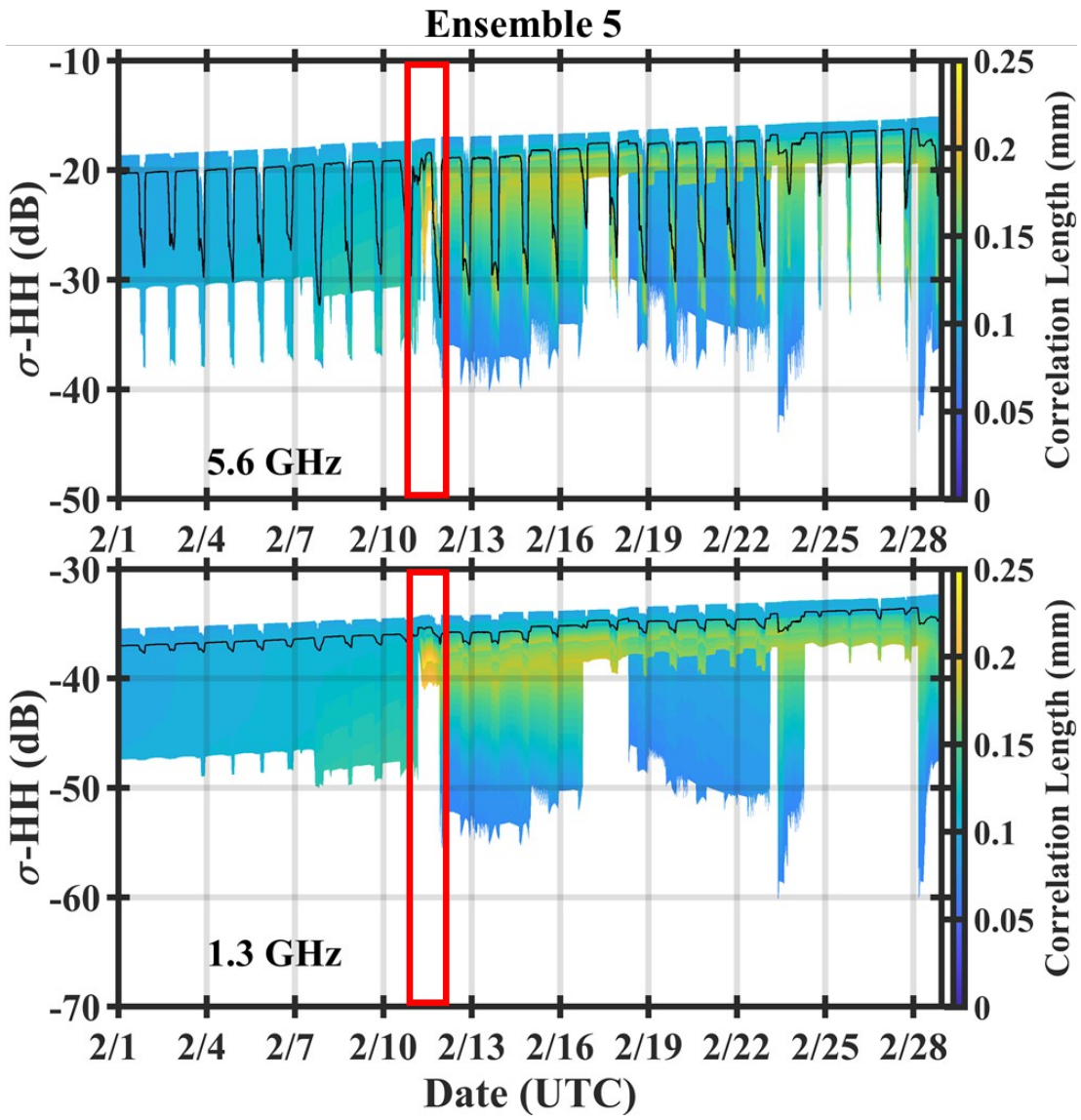

603

604 **Figure 14.** Temporal evolution of Ensemble 5 backscattering coefficients σ-HH at 5.6 GHz (top
605 panel) and 1.3 GHz (bottom panel) contoured by correlation length of the snowpack top layer. The
606 black line is the Ensemble 5 mean. The red box marks the overnight period from 2/10/2017 to
607 2/11/2017 followed by daytime hours. UTC= Mountain Standard Time +7.

608 Interestingly, the amplitude of the impact of surface melting in daytime
609 backscattering is the same across scales. For the case of EFF2 when the downscaled
610 precipitation fields are used at 750 × 750 m^2, there is little sensitivity to the spatial
611 variability of precipitation at 1.3 GHz (not shown), whereas the spatial variability
612 can be as high as 10 dB for 5.6 GHz even when snow depth and SWE differences
613 are small at S2 due to daytime surficial snowpack melting in the second and third
614 weeks of February (Figure S12). Due to cold temperatures, larger spatial variability
615 of snow depth in the end of February does not propagate into the backscattering
616 behavior of the snowpack. Figure 15 contrasts the interplay between snow and
617 rainfall and air temperature at mid-day for the 3-day period 2/20-2/13 when
618 significant spatial variability in mid-day liquid water content in the top layer of the
619 snowpack enhances the spatial variability of backscattering at 5.6 GHz. Whereas
620 there is high sensitivity (~10 K) for passive microwave as illustrated in Figure 16
621 for the same three-day period, there is high ambiguity in the relationship between
622 SWE and Tb, or snow depth and Tb, as a function of time-of-day (e.g., 1.3 GHz)

and especially for the shorter wavelengths (e.g., 5.6 GHz). It is therefore desirable for snow remote sensing to make either active or passive measurements either early in the morning or late in the afternoon.

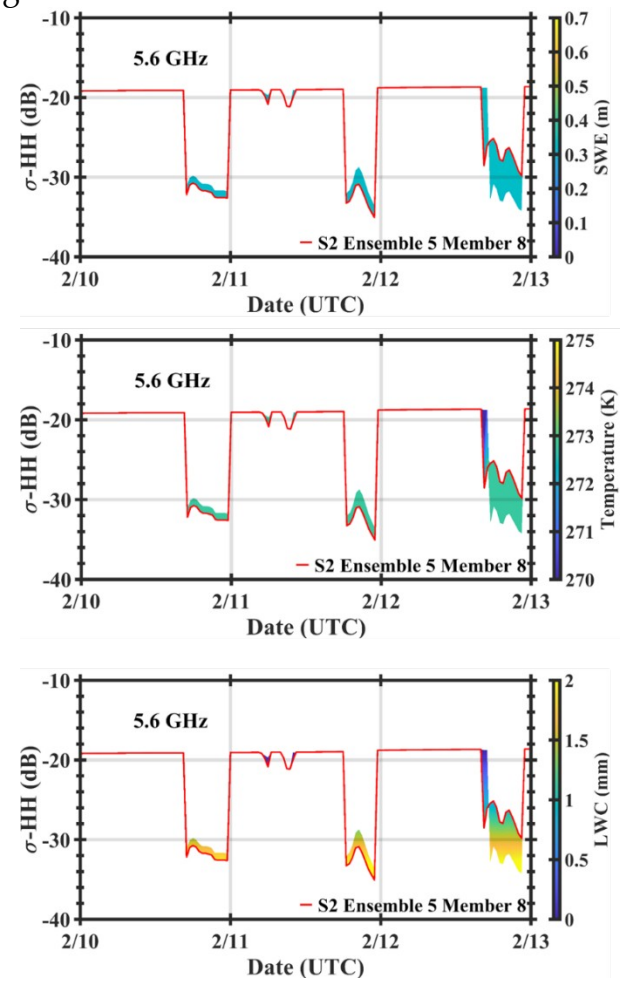

Figure 15. Diurnal cycle of 5.6 GHz σ-HH contoured by SWE (top panel), and temperature (mid-panel) and liquid water content (LWC, bottom panel) of the top layer of the snowpack at S2 over the period 2/10-2/13 for EFF2 (table 3). The ~ 10dB range on 2/12 results from compounding nonlinear effects of modest sub-grid-scale variability of snow depth (Fig. S12) and mid-day temperatures above the freezing level that cause melting at the snowpack surface. UTC=Mountain Standard Time +7.

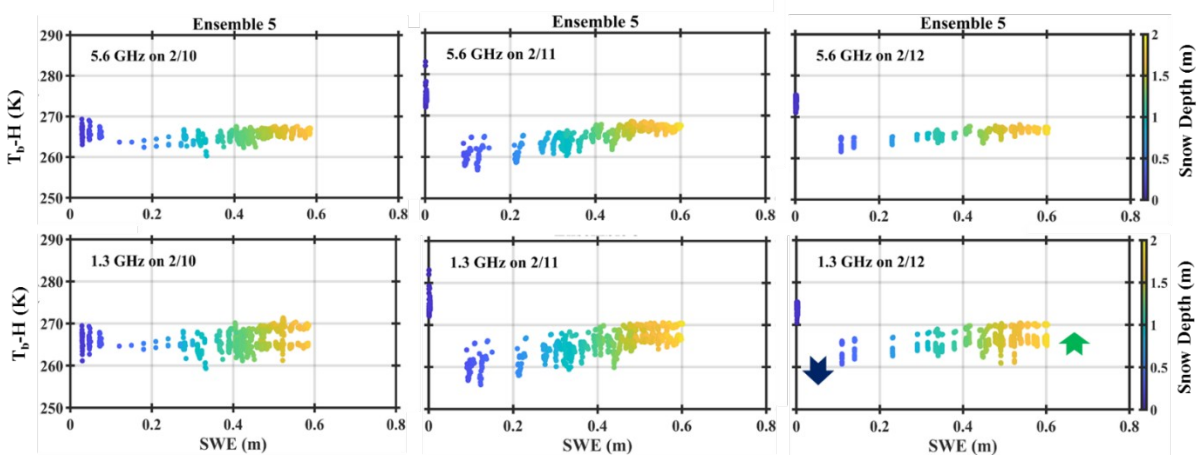

Figure 16. Diurnal cycle of brightness temperature Tb-H at 1.3 GHz (bottom row) and 5.6 GHz (top row) for all Ensemble 5 members thus capturing the spatial variability of the snowpack across the Grand Mesa during the warm weather period 2/10-2/23 from left to right. Note snowpack disappearance for some ensemble members (SWE =0) on 2/11 (e.g., Figure 13) and 2/12 due to melt. The high ambiguity (spatial variance) introduced by the local meteorology is apparent with multiple SWE values for each Tb at 5.3 GHz, in particular for intermediate and deep snow and during daytime. The green arrow indicates the direction of Tb increase during nighttime cooling and refreezing the snowpack; the dark blue arrow indicates the direction of Tb decrease during daytime warming with substantial surficial melting.

Figure 17 shows the simulated temporal evolution of Ensemble 5 mean σ-HH at 1.3 GHz at 7 AM MST from 1/1 through 2/28 in 2017 in terms of total snow accumulation and day–to-day changes. The corresponding results at 5.6 GHz are shown in Figure S13. The snowpack deepens in January due to cold weather and several snowstorms in January corresponding to an increase in SWE as a function of σ-HH ($\Delta SWE/\Delta\sigma$) of 5-6 cm/dB at the monthly time-scale. The erratic weather in February, results in much lower snow accumulation with rapidly changing backscatter in the first week of the month mainly attributed to microphysical changes in the top layer of the snowpack, followed by steady accumulation at a rate of ~2 cm/dB later in the month. This behavior demonstrates the time-integrated sensitivity of backscatter to regional weather during the accumulation phase of the seasonal snowpack. It implies that the specific history of weather and snowpack interactions determines the backscattering behavior, and it hints therefore at the necessity of physically-based retrieval via for example data-assimilation for applications over large areas. Yurchak [49] relates ($\Delta SWE/\Delta\sigma$) to the variance of the Fresnel coefficient in a layered snow medium, which in turn is proportional to the density variance in the snow medium. This approach can be used to explain the spatial variability of accumulation rates (2-10 cm/dB) from scatterometer data matching different types of snow in Greenland [26]. Using a 1-layer snow model and one-parameter at a time sensitivity analysis, Oveigharan et al. [50] showed that the backscattered power in dual polarization dual frequency retrievals at C- and Ku-bands is more sensitive to snow density and grain radius rather than to snow depth. This raises the question of the possibility to retrieve information on snowpack stratigraphy. Furthermore, the time-matched history of consecutive changes in SWE (ΔSWE) and changes in backscatter ($\Delta\sigma$-HH) in Figure 17 and Figure S13 suggests that it is possible to use changes in backscatter to detect individual snowstorm activity and associated snowfall above a minimum thresholds of $\Delta\sigma$ (~0.3 dB/day).

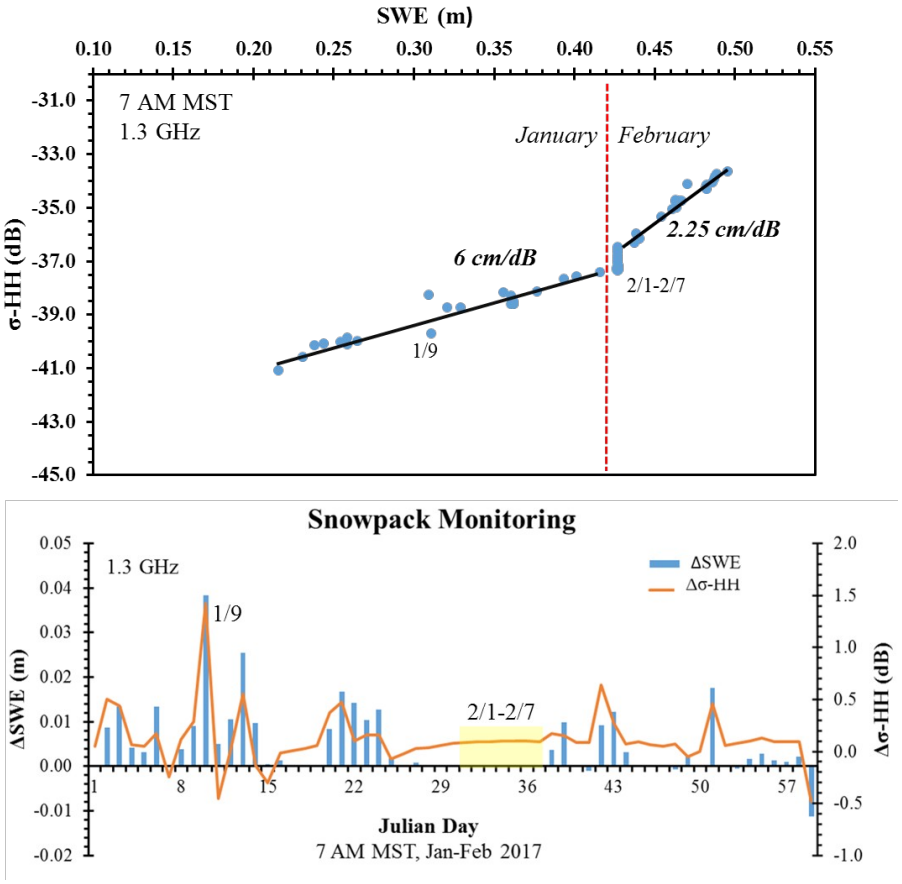

672

673 **Figure 17.** Snowpack monitoring in Grand Mesa at 1.3 GHz HH-pol during the accumulation
674 season, January-February 2017. **Top** — Heuristic linear relationship between snowpack
675 accumulation and backscatter ($R^2 > 0.95$) that reflects the integration of variable weather conditions
676 in January and February in the simulated snowpack. **Bottom** — SWE and backscatter increments,
677 respectively ΔSWE and Δσ-HH, are calculated as the difference between today's and yesterday's
678 values at 7AM MST. MST- Mountain Standard Time = UTC-7.

679 The full evolution of the Ensemble 5 mean of simulated backscatter and
680 brightness temperatures of the seasonal snowpack across Grand Mesa is shown
681 respectively in Figure 18a and 18b from 9/1/2016 through 6/30/2017 for different

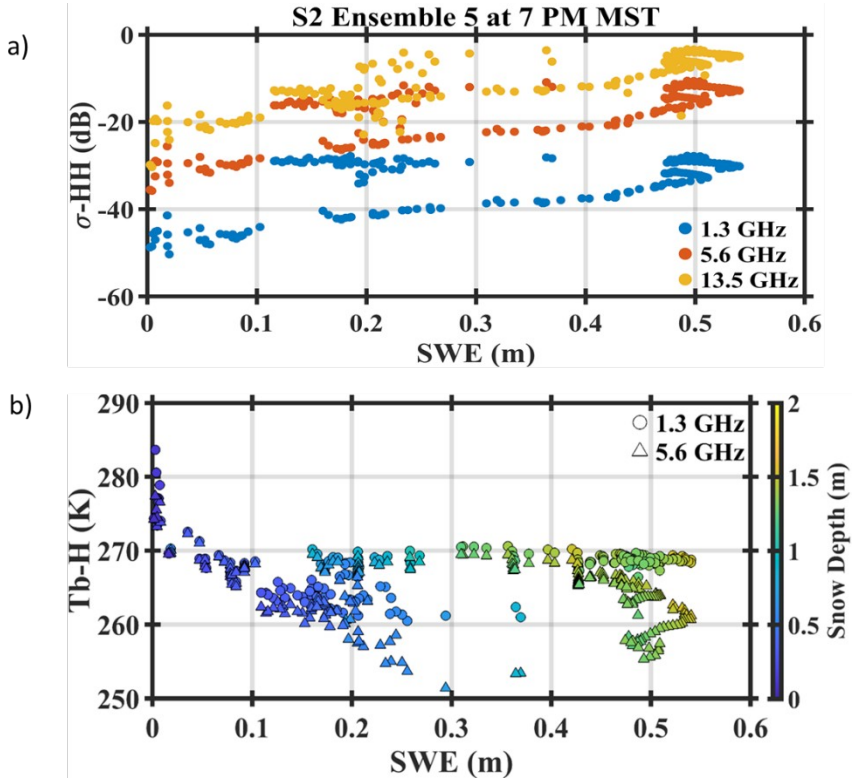

682 frequencies and time-of-day. Results for different polarizations at 7 AM MST, and
683 even at mid-day albeit complicated by mid-day melting exhibit similar behavior
684 (Figure S14).
685

686 **Figure 18. a)** Seasonal evolution of Ensemble 5 mean backscatter at 7PM MST across the Grand
687 Mesa throughout the snow season from 9/1/2016 through 6/30/2017. Overall behavior is similar
688 for all polarizations. **b)** Seasonal evolution of Ensemble 5 mean brightness temperatures at 7PM
689 MST across the Grand Mesa throughout the snow season from 9/1/2016 through 6/30/2017.
690 Overall behavior is similar for all polarizations. MST- Mountain Standard Time = UTC-7.

691 The temporal evolution of backscatter data show hysteresis between the
692 accumulation and the melt phase is synthesized by the conceptual diagram in
693 Figure 19a. Evidence of nonlinear behavior is apparent in the winter-spring
694 transition season with melt-refreeze cycles (April), and in the melt regime for deep
695 snow as the snowpack ripens (May) and for ripe shallow snowpack conditions late
696 in the season (June). Hysteretic backscatter offsets decrease with frequency
697 increases, and essentially collapse at Ku-band in the melt regime for which case
698 sensitivity to small changes in wet shallow snowpacks introduce large uncertainty
699 (i.e., noise). Although the range of conditions simulated here is limited by model
700 simplicity and strict focus on uncertainty tied to meteorological forcing and not to
701 model structure or model parameters, the results suggest that there is potential to
702 take advantage of hysteresis at lower frequencies (e.g., L- and C-band in the melt
703 regime) and power at higher frequencies (e.g., Ku-band in the accumulation
704 regime) to improve the signal-to-noise ratio in SWE remote sensing.
705 The temporal evolution of microwave emissions maps a closed trajectory (e.g.,
706 limit-cycle) in the (Tb, SWE) phase-space that shows very little sensitivity during
707 the accumulation phase when SWE > 10 cm followed by large nonlinear sensitivity
708 in the return phase with clear separation of the behavior of deep snow in early
709 winter-spring transition and shallow snow in late spring. Further, the limit-cycle at
710 13.5 GHz in Figure 18b (13.5 GHz) shows high sensitivity to melt-refreeze cycles at
711 7 PM in the winter-spring transition that are not apparent at 1.3 GHz. This reflects
712 the freezing of daily melt, in contrast with the limit-cycle at mid-day (Figure S15)
713 where the presence of liquid water in the top layer of the snowpack makes the 13.5
714 GHz brightness temperatures limit-cycle behave like the 1.3 GHz limit-cycle albeit
715 with wider hysteretic offset. This behavior is synthesized in the conceptual
716 diagram in Figure 19b. The transient cooling in early spring followed by warming
717 in late spring is well documented in [21] for brightness temperatures at higher
718 frequencies (up to 37 GHz), and the differences in the hysteretic offsets at different
719 frequencies provide a physical basis for early heuristic remote sensing algorithms
720 [15,16]. Because of dynamic nonlinear sensitivity and dramatic changes between
721 early and late melt regimes, and because of sensitivity to seasonal weather at local
722 and regional scales (e.g., Figure 17), finding unique relationships for retrieval is
723 challenging (i.e., calibration of model parameters). Nevertheless, coupling of snow
724 hydrology and microwave models provides a framework for physically-based
725 interpretation and disambiguation of microwave measurements of snowpack
726 properties toward a monitoring system that can be achieved by data-assimilation.

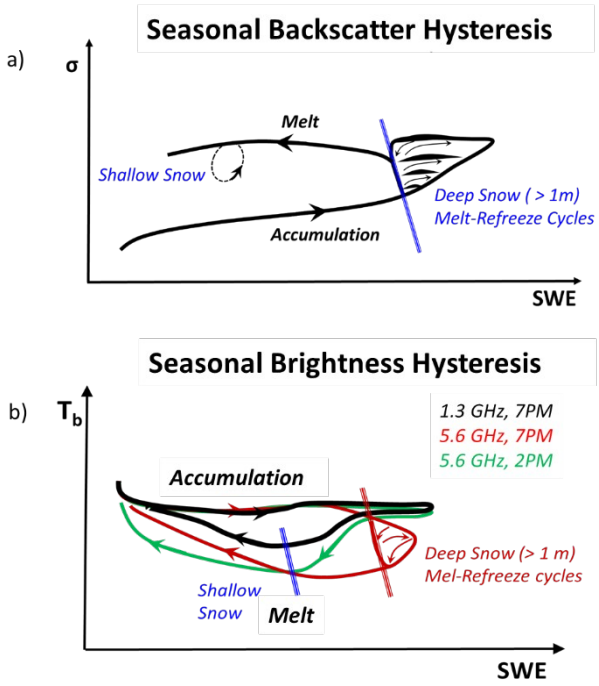

Figure 19. Conceptual synthesis of microwave hysteresis: **a)** Synthesis of seasonal snowpack backscatter behavior as a function of SWE exhibiting hysteresis between accumulation and melt phases at L- and C-bans (e.g. 1.3 and 5.6 GHz). Hysteresis is not present at Ku-band (e.g., 13.5 GHz) and higher frequencies; **b)** Synthesis of seasonal brightness behavior as a function of SWE exhibiting hysteresis between accumulation and melt phases at L- and C-bands.

5. Synthesis and Conclusion

Ensemble predictions of the seasonal snowpack over Grand Mesa, CO were conducted for the hydrologic year 2016-2017 using a multilayer snow hydrology model coupled to a microwave emission model. Atmospheric forcing ensembles were designed based on atmospheric reanalysis at 3-5km spatial resolution and exploratory simulations were conducted using fractal-downscaled precipitation between 3 km and 750 m. SWE and snow depth predictions driven by HRRR atmospheric forcing (EFF1, Ensemble 5; Table 1) at 3 km resolution show good agreement with snowpit observations. Despite neglecting topographic and land-cover variations across the Grand Mesa, the local bias SWE predictions are generally less than 50 mm (< 10% actual SWE, Figure 10 top panel) except at S1 and VS, where steep slopes and strong winds are expected to play an important role in snow redistribution. Although the effect of uncertainty in snowfall, air temperature and wind redistribution is apparent in the assessment of global bias (Figure 10 bottom panel), the modified Willmott Agreement Index (Appendix C) [51] that measures the agreement between the spread of the observations and model predictions is generally above 0.8, which is indicative of robust skill in space and time. The model performance meets with advantage the desired requirements for global observations from space by the Decadal Survey of Earth Sciences and Applications from Space [46], that is 10% uncertainty in SWE 3-5 km resolution, and thus it is suitable to examine the uncertainty propagation from meteorological forcing to snowpack states to radiometric and scattering behavior with an eye toward remote sensing of SWE. Ultimately, the goal is to be able to separate uncertainty in snowpack measurements from space (backscattering coefficient and brightness temperatures) from retrieval ambiguity tied to spatial scale, snow hydrology regime, and snowpack heterogeneity.

The signatures of the sub-seasonal variability of snow physics were investigated through forward modeling akin of an exploratory observing system simulation experiment (OSSE) in Grand Mesa. Specifically, the co-evolution of radar backscattering coefficients and brightness temperatures at L- (1.3 GHz), C- (5.6 GHz), Ku- (13.5 GHz), and Ka- (37.5 GHz) bands was examined during snow accumulation and melting phases toward assessing their interpretability and sensitivity. At daily time-scales during the accumulation season the sensitivity to atmospheric forcing (i.e., spatial variability of weather within the Grand Mesa) remains below 3 dB for cold weather conditions (i.e., dry snow), and increases to 8-10 dB at mid-day when temperatures rise above freezing in the presence of surficial melt. Sub-grid scale variability of precipitation at 750 m in this study had a modest impact on snow depth, SWE and backscatter in the accumulation regime for dry snow. However, microwave sensitivity increases by as much as 300% as small differences in snowpack vertical structure are amplified when liquid water content is present. Therefore, surficial melting is the process governing backscatter sensitivity to sub-grid scale variability. At mid-day this sensitivity amounts to 3-10 dB of uncertainty measured by the standard deviation of the ensemble backscatter in Grand mesa, but it can be constrained below 3 dB if measurements are made early in the morning or late in the afternoon. Intermittent melt coupled with spatial variability of snow accumulation explains the wide range of the ensemble (~20 dB).

At monthly time-scales during the accumulation season, robust linear heuristic functional relationships between ensemble mean backscatter and SWE can be found across the Grand Mesa (e.g., ~5-6 cm/dB in January; ~2-2.5 cm/dB in February at L- and C-bands). The nonstationary of these functional relationships reflects the cumulative impact of atmosphere-snowpack interactions over time, in particular melt-refreeze cycles that modify the microphysical and thermodynamic structure in the top 50 cm of the snowpack. This finding is consistent with conclusions by [9] using C-band SAR measurements from Sentinel-1.

Analysis of full seasonal simulations reveals hysteresis in the mean backscatter behavior between accumulation and melt phases with hysteretic offsets that become noisier as frequency increases especially for shallower and ripe snowpacks in late spring. The hysteretic behavior is captured as well by the temporal evolution of microwave emissions, with brightness temperatures following very distinct trajectories in the melt regime for deep and shallow snowpacks. These physical ties between snow hydrology and microwave behavior provide a physics-based framework to increase the potential for remote sensing of SWE through physical disambiguation of remotely-senses microwave behavior. For instance, a multi-frequency approach to SWE measurement conditional on snow state could consist of using Ku-band and brightness temperatures during the accumulation regime, and C- and, or L-band in the melt regime. It also provides a framework for active-passive sensing for instance by making use of passive sensing in the accumulation regime to detect freeze-melt cycles (e.g., different between day-to-day changes in L- band backscatter and L-band brightness temperatures) and, or using active C-band or L-band in the early spring, followed by passive in the late spring.

Sub-grid scale effects of topography, land-cover and in particular forests, are not explicitly addressed in this study, and a key question is whether compound uncertainty remains below 3 dB at the Grand Mesa scale (~300 km^2) and ~10 km^2 resolution and, or alternatively their backscatter contribution can be isolated and parameterized. In the melt regime, independently of spatial scale and sub-grid scale variability, snow wetness alone introduces large ambiguities that can be addressed by probing the other snowpack states resolved in the snow hydrology model. Therefore, a coupled snow hydrology-radiative transfer approach should be advantageous toward global systematic implementation of SWE retrieval.

Although more systematic evaluations are needed to inform snow remote sensing, one important implication of these results is that calibrated empirical or semi-empirical retrieval algorithms are not transferable from one location to another, or from one season to another. Note that only a limited number of frequencies and polarizations is fully analyzed in this study, but the framework can be implemented using other radiative transfer models and is suitable to systematically explore realistic remote-sensing architectures. One practical advantage of active-passive combinations is the development of straightforward error models for data-assimilation given the unambiguous relationships between snowpack properties and the microwave signal.

Supplementary Materials: The following are available online at www.mdpi.com/xxx/s1, **Figure S1a.** Numbering order convention for HRRR grids in Figure 1 (right panel) corresponding to the ID numbers in Table S1. **Figure S1b.** Illustration of overlap of several HRRR Grids with one ECMWF grid including hypothetical distribution of SNOWEx'17 snowpits within ECMWF grid. The diamonds are placed at the center of each grid. **Figure S2.** Structure of 1-D MHSM workflow. The first snowpack layer forms when the following two conditions are met: (1) The air temperature is below the freezing point (273.15 K); and (2) precipitation is present. In the melting season, liquid precipitation is added the snowpack's melting outflow directly. **Figure S3.** Geometry of the layered snowpack with an electromagnetic wave incident from above at an incidence angle θ_n [36]. Notation: layer thickness d_j, layer temperature T_j, transmissivity t_j, volume reflectivity r_j, emissivity e_j, and interface reflectivity s_j, refracted angle θ_{j-1} for layer number j ranging from 1 (bottom) to n (top), snow-ground reflectivity s_0 and ground temperature T_0. [$e_j+r_j+t_j=1$ as required by energy conservation]. **Figure S4.** Schematic view of incoming and outgoing radiation between adjacent snow layers in MEMLS [36]. Notation as in Figure S2. **Figure S5.** Illustration of recursive fractal precipitation downscaling scheme from 3 km (HRRR resolution) to 750 m. At each stage 50 fields are generated, but only the ensemble mean is downscaled to the next stage. Finally, each of 16 ensemble means at 750 m resolution is used to generate a member of EFF2 for each ECMWF pixel. **Figure S6.** MHSM predicted time-varying snowpack stratigraphy in terms of number of layers and depth of top layer during February 2017 corresponding to results presented in Figures 10 and 11 for EFF1 Ensemble 5: a) ensemble member 8 at S2; b) ensemble member 13 at SD3; and c) ensemble member 29 at S5. The time-series are plotted in UTC = LST + 7. **Figure S7.** MSHM predicted time-series of temperature in the upper two layers of the snowpack (top row) and snowpack surface heat flux (bottom row) at S2 for EFF1 Ensemble 5 Member 8. Specified air temperature from the HRRR model at grid 8 (Figure S1a) is provided for reference. The time-series are plotted in UTC = LST + 7. **Figure S8.** HRRR incoming longwave radiation flux during February 2027 at Grid 8 (Figure S1a). Time-series are plotted in UTC = LST + 7. **Table S1.** Geographical correspondence between ECMWF and HRRR grids in Figure 1. **Table S2.** ECMWF reference grid S2: HRRR grid points (center of HRRR grid cell) and snowpit locations. Bold red letters identify the HRRR grid ID (Figure S1) nearest to the ECMWF grid center point. **Table S3.** Same as Table S2, but for ECMWF reference grid SD3. **Table S4.** Same as Table S2, but for ECMWF reference grid S5. **Table S5.** Same as Table S2, but for ECMWF reference grid Ex. **Table S6.** Same as Table S2, but for ECMWF reference grid S1. **Table S7.** Same as Table S2, but for ECMWF reference grid S3. **Table S8.** Same as Table S2, but for ECMWF reference grid S4. **Table S9.** Same as Table S2, but for ECMWF reference grid SD2. **Table S10.** Same as Table S2, but for ECMWF reference grid VS.

Author Contributions: A.B. designed the research and analysis; Y.C. processed data, carried out model simulations, and conducted quantitative analysis under the guidance of A.B.; A.B. and Y.C. wrote the manuscript cooperatively. All authors have read and agreed to the published version of the manuscript.

Funding: This research was funded by NASA's Terrestrial Hydrology Program under NASA grant NNX17AL44G with the corresponding author.

Acknowledgments: The authors appreciate the National Snow & Ice Data Center for providing the NASA 2017 SnowEx data and all the colleagues who worked on the field campaign to collect the valuable data sets.

Conflicts of Interest: The authors declare no conflict of interest.

Appendix A: The Multilayer Snow Hydrology Model (MSHM)

The MSHM simulates snow hydrological processes in the snowpack column and quantifies energy and water fluxes at the land-atmosphere interface driven by meteorological forcing. The flowchart of model components and how they are connected is depicted in Supplementary Figure S1. The model formulation used in this manuscript is described here; additional implementation details and alternative parameterizations can be found in [20,21]. Each variable's unit is in ().

A.1 Compaction

When SWE changes due to snowmelt, sublimation, rain-on-snow events, and snowfall, the snow depth h_{snow} (m) is decreased by the compaction ratio CR (1/s) that is parameterized with metamorphism and overburden effects as follows:

$$CR = \left| \frac{1}{h_{snow}} \frac{d\Delta h_{snow}}{dt} \right|_{metamorphism} + \left| \frac{1}{h_{snow}} \frac{d\Delta h_{snow}}{dt} \right|_{overburden} \quad (A1)$$

$$\left| \frac{1}{h_{snow}} \frac{d\Delta h_{snow}}{dt} \right|_{metamorphism} = -2.778 \times 10^{-6} \times C \times e^{-0.04 \times (T_{snow} - T_i)} \quad (A2)$$

$$\left| \frac{1}{h_{snow}} \frac{d\Delta h_{snow}}{dt} \right|_{overburden} = \frac{-P_{snow}}{\eta} \times e^{-0.08 \times (T_{snow} - T_i)} \times e^{-0.021 \times \rho_{snow}} \quad (A3)$$

where

$$C = \begin{cases} 1 & \rho_{snow} \le 150\, kg/m^3 \\ 2 \times e^{-0.046 \times (\rho_{snow} - 150)} & \rho_{snow} > 150\, kg/m^3 \end{cases} \quad (A4)$$

η is the viscosity coefficient at T_i (¿ $273.15\,K$), P_{snow} is the pressure due to the snowpack weight (N/m^2), ρ_{snow} and T_{snow} are the snow density (kg/m^3) and temperature (K), respectively.

A.2 Snowpack Temperature

The heat energy transfer equation is

$$c_{snow} \times \rho_w \times h_{swe} \times \frac{\partial T_{snow}}{\partial t} = K_{snow} \times \frac{\partial T_{snow}}{\partial z} + \phi \quad (A5)$$

in which ρ_w (¿ $1000\,kg/m^3$) is the water density, c_{snow} is the specific heat capacity of the snowpack (J/kg/K), and heat conductivity of the snowpack K_{snow} (W/m/K) is calculated by

$$K_{snow} = K_a + \left(7.75 \times 10^{-5} \times \rho_{gs} + 1.105 \times 10^{-5} \times \rho_{gs}^2\right) \times \left(K_i - K_a\right) \quad (A6)$$

where K_i and K_a are, respectively, the heat conductivity of ice and air (W/m/K), ρ_{gs} is the snow density weighted by SWE h_{swe} (m) and liquid water content LWC (m):

$$\rho_{gs} = \rho_{snow} \times \frac{h_{swe} - LWC}{h_{swe}} \quad (A7)$$

903 External forcing term ϕ (W/m^2) is null except at the bottom and at the top layer
904 of the snowpack. For the bottom layer:

905 $$\phi = K_{ss} \times \frac{T_{soil} - T_{snow}}{h_{soil} + h_{snow}} \quad (A8)$$

906

907 K_{ss}, T_{soil} and h_{soil} are the heat conductivity of interacted snow-soil system
908 (W/m/K), superficial soil temperature (K) and soil depth (m), respectively. For
909 the top layer:

910

911 $$\phi = NSR + NLR + S + L \quad (A9)$$

912

913 the net shortwave radiation flux NSR (W/m^2) and the net longwave radiation flux
914 NLR (W/m^2) equal to

915 $$NSR = SW \times (1 - Alb) \quad (A10)$$

916 $$NLR = LW - \varepsilon \times \sigma \times T_{snow}^4 \quad (A11)$$

917

918 SW and LW are the downward shortwave and longwave radiation flux (W/m^2),
919 Alb and ε are the surface albedo and emissivity, respectively, and σ is the Stefan-
920 Boltzmann constant.
921 Then, the sensible heat flux S (W/m2) is estimated by the air specific heat
922 capacity c_a (J/kg/K), air density ρ_a (kg/m3), air temperature T_a (K) and windspeed
923 U (m/s) like:

924

925 $$S = c_a \times \rho_a \times CDT \times U \times (T_a - T_{snow}) \quad (A12)$$

926

927 while the latent heat flux L (W/m^2) is the product of air density, latent heat of
928 vaporization L_v (J/kg) and sublimation rate S (m/s):

929

930 $$L = \rho_a \times L_v \times S \quad (A13)$$

931 and S is adapted by the Penman-Monteith equation:

932

933 $$S = \frac{\Delta \times (NSR + NLR) + \gamma \times L_v \times \rho_a \times CDT \times U \times (q_a - q^{¿}_{snow})}{\rho_w \times L_v \times [\Delta + \gamma \times (1 + CDT)]} \quad (A14)$$

934

935 where q_a is the specific humidity (kg/kg) of air and Δ (Pa/K) that is the slope of
936 saturation-vapor versus temperature curve at the air temperature can be
937 approximated as:

938

939 $$\Delta = \frac{e^{¿}_{snow} - e^{¿}_a}{T_{snow} - T_a} \quad (A15)$$

940

of which the saturated vapor pressure of snow $e^{¿}_{snow}$ and air $e^{¿}_{a}$ are expressed similarly:

$$e^{¿}_{snow}=611.2\times\exp¿$$

$$e^{¿}_{a}=611.2\times\exp¿$$

The psychrometric constant γ (Pa/K) and the snowpack's saturated specific humidity $q^{¿}_{snow}$(kg/kg) are calculated by

$$\gamma=\frac{c_a\times P_a}{0.622\times L_v} \quad (A18)$$

$$q^{¿}_{snow}=0.622\times\frac{e^{¿}_{snow}}{P_a} \quad (A19)$$

where P_a (Pa) is the air pressure.

A.3 Conductance Factor and Aerodynamic Drag Coefficient

The parameterization of the conductance factor CDT in Equation (A11) and (A13) is like:

$$CDT=\frac{1}{R_{snow}+\frac{1}{A}} \quad (A20)$$

of which the snow surface resistance R_{snow} is defined as a piecewise function of SW:

$$R_{snow}=\begin{cases}100 & SW\geq 50\,W/m^2\\ 1000 & SW<50\,W/m^2\end{cases} \quad (A21)$$

and aerodynamic drag coefficient A is from Louis, 1979:

$$A=\frac{0.16}{\left(\ln\frac{z}{z_r}\right)^2}\times\left(1-\frac{b\times R_i}{1+c\times\sqrt{R_i}}\right) \quad (A22)$$

here z (m) is the height at which the windspeed U is and z_r (m) is the roughness height of snow; b and c are coefficients depending on stability conditions: $b=1$ and $c=4.7$ when the boundary layer is stable (R_i>0.25); whereas $b=9.4$ and

$$c=5.3\times\frac{0.16}{\left(\ln\frac{z}{z_r}\right)^2}\times b\times\sqrt{\frac{z}{z_r}} \quad (A23)$$

for unstable boundary layer ($R_i\leq 0.25$).

971 Besides, the Richardson number R_i is given by

$$R_i = \frac{9.81 \times z \times (\theta_a - \theta_{snow})}{U^2 \times \frac{\theta_a + \theta_{snow}}{2}} \quad (A24)$$

973 of which θ_a and θ_{snow} are the potential temperature (K) of air and top layer snow,
974 which are calculated as follows (1.02×10^5 Pa is the standard atmospheric pressure):
975

$$\theta_a = T_a \left(\frac{1.02 \times 10^5}{P_a} \right)^{0.286} \quad (A25)$$

$$\theta_{snow} = T_{snow} \left(\frac{1.02 \times 10^5}{P_a} \right)^{0.286} \quad (A26)$$

978 *A.4 Melt*

979 Snowpack melting is triggered when the energy need to melt snowpack (Q_{melt})
980 exceeds 0, and Q_{melt} (J/m²) is the sum of the net heat flux $NHFL$ and the snowpack
981 "cold content" Q_{cc}:
982

$$Q_{melt} = NHFL + Q_{cc} \quad (A27)$$

984
985 where $NHFL$ (J/m²) is the product of the MSHM's time step size Δt (s) and forcing
986 terms on the right hand side of Equation (A4):
987

$$NHFL = \Delta t \times \left(K_{snow} \times \frac{\partial T_{snow}}{\partial z} + \phi \right) \quad (A28)$$

989
990 while Q_{cc} (J/m²) is written as:
991

$$Q_{cc} = c_{snow} \times \rho_w \times h_{swe} \times (T¿¿snow - T_i)¿ \quad (A29)$$

993
994 Furthermore, the melting occurs in two phases: ripening and deep melting, for
995 which the snowpack both becomes isothermal (i.e., $T_{snow} = T_i$) and the criteria is
996 based on the difference between Q_{melt} and Q_{ripen} (J/m²) which is the energy need to
997 ripen the snowpack:
998

$$Q_{ripen} = L_m \times \rho_w \times LWC_{max} \quad (A30)$$

1000
1001 here L_m (J/kg) is the latent heat for melting and LWC_{max} (m) that depends on ρ_{snow}
1002 and h_{snow} is the maximum liquid water content retained in the pore spaces against
1003 gravity by surface tension forces of snow grains:
1004

$$LWC_{max}=\begin{cases}0.01\times h_{snow} & \rho_{snow}<400\,kg/m^3\\ \left(0.25\times\dfrac{\rho_{snow}}{\rho_w}-0.099\right)\times h_{snow} & \rho_{snow}\geq 400\,kg/m^3\end{cases} \quad (A31)$$

Ripening happens when $Q_{melt}<Q_{ripen}$, under which there is no water melting out and the internal LWC is proportional to LWC_{max}:

$$LWC=LWC_{max}\times\frac{Q_{ripen}-Q_{melt}}{Q_{ripen}} \quad (A32)$$

On the contrary, deep melting takes place and initiates the meltwater h_{melt} (m):

$$h_{melt}=\frac{Q_{melt}-Q_{ripen}}{L_m\times\rho_w} \quad (A33)$$

by which the diminution of SWE Δh_{swe} (m) and LWC are determined:

$$\Delta h_{swe}=\begin{cases}h_{swe} & h_{melt}\geq h_{swe}\\ h_{melt}-LWC_{max} & LWC_{max}\leq h_{melt}<h_{swe}\\ 0 & h_{melt}<LWC_{max}\end{cases} \quad (A34)$$

$$LWC=\begin{cases}0 & h_{melt}\geq h_{swe}\\ LWC_{max} & LWC_{max}\leq h_{melt}<h_{swe}\\ h_{melt} & h_{melt}<LWC_{max}\end{cases} \quad (A35)$$

Note the liquid water capacity is reached on the second condition, hence Δh_{swe} is actually the infiltration or runoff released from the snowpack, and the snowpack is completely melted in the first case ($h_{melt}\geq h_{swe}$), so there is no LWC left; whereas all meltwater is held within the snowpack in the last one.

A.5 Rain-on-Snow

Rain-on-snow event only occurs when rainfall rate P_r is not nil and air temperature T_a is above freezing point (T_i), in which case only the top-layer snow will be influenced and its status is dependent of the thermodynamic energy of snowpack (E_{snow}) and rain (E_{rain}), both of which consist of different components:

$$E_{snow}=\underbrace{Q_{cc}+Q_{ripen}}_{H_{ripen}}+\underbrace{L_m\times\rho_w\times h_{swe}}_{H_{melt}} \quad (A36)$$

where H_{ripen} (J/m^2) and H_{melt} (J/m^2) is the heat released from the rain to ripen and melt the snow layer, respectively.

$$E_{rain} = c_w \times M_r \times \underbrace{(T¿¿a - T_i)}_{Q_{wc}} + \underbrace{L_m \times M_r}_{H_{fro}} ¿ \quad (A37)$$

here Q_{wc} (J/m^2) is the "warm content" of the rainfall and H_{fro} (J/m^2) is the released heat after the rain drop becomes totally frozen. c_w is the specific heat capacity of water (J/kg/K) and M_r is the rainfall mass (kg/m^2) during a model's time step (i.e., the product of P_r and Δt).

The warm rainfall would melt the top-layer snow completely in two cases: $E_{rain} \geq E_{snow}$ or $H_{ripen} \leq E_{rain} < E_{snow}$, under both circumstances falling rain joins the snowpack's melting outflow directly. On another hand, when $E_{rain} \leq Q_{cc}$, all rain freezes and adds to the snowpack mass with releasing energy to arise the snowpack temperature by ΔT_{snow} (K):

$$\Delta T_{snow} = (T_i - T_{snow}) \times \left(\underbrace{\frac{E_{rain}}{Q_{cc}}}_{1} + \underbrace{\frac{\frac{M_r}{\rho_w} \times \rho_i}{h_{swe} \times \rho_w}}_{2} \right) \quad (A38)$$

among which 1 and 2 marking the fractional increase toward T_i are the adjusting term of energy and mass, respectively; while the boxed item is actually the increment of snow mass (SWE). ρ_i is the ice density (kg/m^3).

If $E_{rain} < H_{ripen}$ or $Q_{wc} \geq Q_{cc}$, the rain will be absorbed by the isothermal mushy snowpack and promote h_{swe} by the same magnitude in Equation (A38), as well as LWC by ΔLWC (m):

$$\Delta LWC = min\left(\frac{M_r}{\rho_w}, LWC_{max} - LWC \right) \quad (A39)$$

A.6 Dividing and Combining Snow Layers

The MSHM will activate the dividing mechanism which only separates the top-layer snow into $n+1$ new layers and specifies their properties, without acting on the lower layers beneath the top one, if the round ratio (n) of top-layer SWE to a specific threshold ($Thres$) is greater than 1:

$$n = floor\left(\frac{h_{swe}}{Thres} \right) \quad (A40)$$

in which the *floor* operation rounds the fraction to the nearest integer less than or equal to it.

As presented in Figure S2, the snow properties from the layer m to $m+n$ remain the same with the original top layer after the dividing behavior:

$$\rho_{snow}^{m+n} = \ldots = \rho_{snow}^{m+1} = \rho_{snow}^{m} \quad (A41)$$

$$T_{snow}^{m+n}=\ldots=T_{snow}^{m+1}=T_{snow}^{m} \quad (A42)$$

$$L_c^{m+n}=\ldots=L_c^{m+1}=L_c^{m} \quad (A43)$$

except for snow depth and SWE:

$$h_{snow}^{m+n-1}=\ldots=h_{snow}^{m+1}=H_{snow}^{m}=\frac{Thres\times\rho_w}{\rho_{snow}^{m}} \quad (A44)$$

$$h_{swe}^{m+n-1}=\ldots=h_{swe}^{m+1}=H_{swe}^{m}=Thres \quad (A45)$$

$$h_{swe}^{m+n}=h_{swe}^{m}-Thres\times n \quad (A46)$$

$$h_{snow}^{m+n}=\frac{h_{swe}^{m+n}\times\rho_w}{\rho_{snow}^{m}} \quad (A47)$$

On the other hand, when the snow depth h_{snow}^{j} at layer j is less than or equal to a critical value, the MSHM will combine all mass-related terms, such as h_{snow}^{j} and h_{swe}^{j}, with the lower layer $j-1$:

$$h_{snow}^{j}¿h_{snow}^{j}+h_{snow}^{j-1} \quad (A48)$$

$$h_{swe}^{j}¿h_{swe}^{j}+h_{swe}^{j-1} \quad (A49)$$

whereas ρ_{snow}^{j}, T_{snow}^{j} and L_c^{j} are averaged and weighted by SWE through two consecutive snow layers:

$$\rho_{snow}^{j}=\frac{h_{swe}^{j}\times\rho_{snow}^{j}+h_{swe}^{j-1}\times\rho_{snow}^{j-1}}{h_{swe}^{j}+h_{swe}^{j-1}} \quad (A50)$$

$$T_{snow}^{j}=\frac{h_{swe}^{j}\times T_{snow}^{j}+h_{swe}^{j-1}\times T_{snow}^{j-1}}{h_{swe}^{j}+h_{swe}^{j-1}} \quad (A51)$$

$$L_c^{j}=\frac{h_{swe}^{j}\times L_c^{j}+h_{swe}^{j-1}\times L_c^{j-1}}{h_{swe}^{j}+h_{swe}^{j-1}} \quad (A52)$$

Appendix B: The Microwave Emission Model of Layered Snowpacks (MEMLS)

MEMLS was developed based on six-flux theory to simulate multiple volume scattering and absorption, which contains radiation trapping resulted from internal reflections and coherent ones between layer interfaces. It was first implemented to simulated brightness temperatures [36] and recently expanded to simulate

backscattering [35]. The latter made their code publicly available, and we use it in this work.

In MEMLS, the snowpack is described as a column consisting of n horizontal layers (j = 1, 2 … n) with flat boundaries at the surface and interfaces between layers. Each layer is characterized by layer thickness, transmissivity, density, reflectivity, emissivity and temperature that determine the observed snowpack brightness temperature T_b given by the sky brightness temperature T_{sky} (Figure S3).

As illustrated by Figure S4, the outgoing radiation (A_j and D_j) from layer j and the incoming radiation (B_j and C_j) can be expressed as follows:

$$A_j = r_j B_j + t_j C_j + e_j T_j \quad (B1)$$

$$D_j = t_j B_j + r_j C_j + e_j T_j \quad (B2)$$

$$B_j = s_{j-1} A_j + (1 - s_{j-1}) D_{j-1} \quad (B3)$$

$$C_j = (1 - s_j) A_{j+1} + s_j D_j \quad (B4)$$

where D_0 (when $j=1$) on the right hand side of Equation (B3) is defined as the ground temperature T_0; while A_{n+1} (when $j=n$) on the right hand side of Equation (B4) is given by the downwelling sky radiation T_{sky}. Similarly, we can derive the main model output — the whole snowpack brightness temperature T_b from

$$T_b = B_{n+1} = s_n T_{sky} + (1 - s_n) D_n \quad (B5)$$

D_n can be determined by substituting Equations (B3) and (B4) into Equations (B1) and (B2):

$$A_j = r_j \left[s_{j-1} A_j + (1 - s_{j-1}) D_{j-1} \right] + t_j \left[(1 - s_j) A_{j+1} + s_j D_j \right] + e_j T_j \quad (B6)$$

$$D_j = t_j \left[s_{j-1} A_j + (1 - s_{j-1}) D_{j-1} \right] + r_j \left[(1 - s_j) A_{j+1} + s_j D_j \right] + e_j T_j \quad (B7)$$

This coupled linear system of equations can be written in matrix form:

$$A = M_1 A + M_2 D + E \quad (B8)$$

$$D = M_3 A + M_4 D + F \quad (B9)$$

among which M_1, M_2, M_3 and M_4 are $n \times n$ matrices including reflectivity r, transmissivity t, and emissivity e; E and F are $n \times 1$ vectors containing boundary T_{sky} and surface temperature T_0.

After linear algebra, the final expression for D is

$$D=\left(I-M_5\right)^{-1}\left[M_3\left(I-M_1\right)^{-1}E+F\right] \quad (B10)$$

where I is the identity matrix and M_5 is

$$M_5=M_3\left[\left(I-M_1\right)^{-1}M_2\right]+M_4 \quad (B11)$$

Appendix C: Modified Wilmott Agreement Index [51]

$$WAI_{d,p}^{local}=1-\frac{\left(y_{d,p}-\overline{x}_{d,p}\right)}{2\times\sqrt{\frac{1}{Ns(d,p)}\sum_{s=1}^{Ns(d,p)}\left(x_{d,p}^{s}-\overline{x}_{d,p}\right)^2+\frac{1}{Nr}\sum_{r=1}^{Nr}\left(\overline{y}_d-\overline{x}_{d,p}\right)^2}} \quad (C1)$$

$$WAI_{d,p}^{global}=1-\frac{\left(\overline{y}_d-\overline{x}_{d,p}\right)}{2\times\sqrt{\frac{1}{Ns(d,p)}\sum_{s=1}^{Ns(d,p)}\left(x_{d,p}^{s}-\overline{x}_{d,p}\right)^2+\frac{1}{Nr}\sum_{r=1}^{Nr}\left(\overline{y}_d-\overline{x}_{d,p}\right)^2}} \quad (C2)$$

$y_{d,p}$ is the model SWE (or snow depth) simulated over the HRRR grid that is nearest to the ECMWF grid point p on day d at time $t = Tref$, where $Tref$ = 10 AM LST = 17:00 UTC;

Nr (=43) is the number of HRRR grids;

$Ns(d,p)$ is the number of snowpits within pixel p on day d, which is different for each pixel p;

$x_{d,p}^{s}$ is the observed SWE (or snow depth) at site s within pixel p on day d;

$\overline{x}_{d,p}$ is the mean of the observations from all sites within pixel p on day d;

$\overline{y}_d$ is the ensemble mean on day d at time $t = Tref$.

References

1. Hall, D.K. Assessment of Polar Climate Change Using Satellite Technology. *Rev Geophys* **1988**, *26*, 26-39.
2. Barnett, T.P.; Dumenil, L.; Schlese, U.; Roeckner, E.; Latif, M. The Effect of Eurasian Snow Cover on Regional and Global Climate Variations. *J Atmos Sci* **1989**, *46*, 661-685.
3. Chapin, F.S.; Sturm, M.; Serreze, M.C.; McFadden, J.P.; Key, J.R.; Lloyd, A.H.; McGuire, A.D.; Rupp, T.S.; Lynch, A.H.; Schimel, J.P., et al. Role of land-surface changes in Arctic summer warming. *Science* **2005**, *310*, 657-660.
4. Gustafsson, D.; Stahli, M.; Jansson, P.E. The surface energy balance of a snow cover: comparing measurements to two different simulation models. *Theor Appl Climatol* **2001**, *70*, 81-96.
5. Lemke, P.; Ren, J.; Alley, R.B.; Allison, I.; Carrasco, J.; Flato, G.; Fujii, Y.; Kaser, G.; Mote, P.; Thomas, R.H. Observations: changes in snow, ice and frozen ground. **2007**.
6. Albert, M.R. Effects of snow and firn ventilation on sublimation rates. *Ann Glaciol-Ser* **2002**, *35*, 52-56.
7. Barnett, T.P.; Adam, J.C.; Lettenmaier, D.P. Potential impacts of a warming climate on water availability in snow-dominated regions. *Nature* **2005**, *438*, 303-309.
8. Painter, T.H.; Skiles, S.M.; Deems, J.S.; Brandt, W.T.; Dozier, J. Variation in Rising Limb of Colorado River Snowmelt Runoff Hydrograph Controlled by Dust Radiative Forcing in Snow. *Geophys Res Lett* **2018**, *45*, 797-808.
9. Manickam, S.; Barros, A. Parsing Synthetic Aperture Radar Measurements of Snow in Complex Terrain: Scaling Behaviour and Sensitivity to Snow Wetness and Landcover. *Remote Sens-Basel* **2020**, *12*.

10. Schmugge, T.J.; Kustas, W.P.; Ritchie, J.C.; Jackson, T.J.; Rango, A. Remote sensing in hydrology. *Advances in water resources* **2002**, *25*, 1367-1385 %@ 0309-1708.
11. Tedesco, M.; Kelly, R.E.J.; Foster, J.L.; Chang, A.T.C. AMSR-E/Aqua daily L3 global snow water equivalent EASE-Grids V002. *National Snow and Ice Data Center: Boulder, CO* **2004**.
12. Lettenmaier, D.P.; Alsdorf, D.; Dozier, J.; Huffman, G.J.; Pan, M.; Wood, E.F. Inroads of remote sensing into hydrologic science during the WRR era. *Water Resour Res* **2015**, *51*, 7309-7342.
13. Hall, D. *Passive microwave studies of snowpack properties*; Goddard Space Flight Center: 1978.
14. Hall, D.; Foster, J.; Chang, A.; Rango, A. Passive microwave applications to snowpack monitoring using satellite data. **1979**.
15. Rango, A.; Chang, A.; Foster, J. The utilization of spaceborne microwave radiometers for monitoring snowpack properties. *Hydrology Research* **1979**, *10*, 25-40.
16. Chang, A.; Foster, J.; Hall, D.K. Nimbus-7 SMMR derived global snow cover parameters. *Annals of glaciology* **1987**, *9*, 39-44.
17. Grody, N.C.; Basist, A.N. Global identification of snowcover using SSM/I measurements. *Ieee T Geosci Remote* **1996**, *34*, 237-249.
18. Tait, A.B. Estimation of snow water equivalent using passive microwave radiation data. *Remote Sens Environ* **1998**, *64*, 286-291.
19. Andreadis, K.M.; Liang, D.; Tsang, L.; Lettenmaier, D.P.; Josberger, E.G. Characterization of errors in a coupled snow hydrology-microwave emission model. *J Hydrometeorol* **2008**, *9*, 149-164.
20. Kang, D.H.; Barros, A.P. Observing System Simulation of Snow Microwave Emissions Over Data Sparse Regions-Part I: Single Layer Physics. *Ieee T Geosci Remote* **2012**, *50*, 1785-1805.
21. Kang, D.H.; Barros, A.P. Observing System Simulation of Snow Microwave Emissions Over Data Sparse Regions-Part II: Multilayer Physics. *Ieee T Geosci Remote* **2012**, *50*, 1806-1820.
22. Kang, D.H.; Barros, A.P.; Dery, S.J. Evaluating Passive Microwave Radiometry for the Dynamical Transition From Dry to Wet Snowpacks. *Ieee T Geosci Remote* **2014**, *52*, 3-15.
23. Tedesco, M.; Kim, E.J.; England, A.W.; De Roo, R.D.; Hardy, J.P. Brightness Temperatures of Snow Melting/Refreezing Cycles: Observations and Modeling Using a Multilayer Dense Medium Theory-Based Model. *Ieee T Geosci Remote* **2006**, *44*, 3563-3573, doi:10.1109/tgrs.2006.881759.
24. Foster, J.L.; Sun, C.J.; Walker, J.P.; Kelly, R.; Chang, A.; Dong, J.R.; Powell, H. Quantifying the uncertainty in passive microwave snow water equivalent observations. *Remote Sens Environ* **2005**, *94*, 187-203.
25. Langlois, A.; Royer, A.; Derksen, C.; Montpetit, B.; Dupont, F.; Goita, K. Coupling the snow thermodynamic model SNOWPACK with the microwave emission model of layered snowpacks for subarctic and arctic snow water equivalent retrievals. *Water Resour Res* **2012**, *48*.
26. Rotschky, G.; Rack, W.; Dierking, W.; Oerter, H. Retrieving snowpack properties and accumulation estimates from a combination of SAR and scatterometer measurements. *Ieee T Geosci Remote* **2006**, *44*, 943-956, doi:10.1109/tgrs.2005.862524.
27. Raleigh, M.S.; Lundquist, J.D.; Clark, M.P. Exploring the impact of forcing error characteristics on physically based snow simulations within a global sensitivity analysis framework. *Hydrol Earth Syst Sc* **2015**, *19*, 3153-3179, doi:10.5194/hess-19-3153-2015.
28. Larue, F.; Royer, A.; De Sève, D.; Roy, A.; Picard, G.; Vionnet, V.; Cosme, E. Simulation and assimilation of passive microwave data using a snowpack model coupled to a calibrated radiative transfer model over northeastern Canada. *Water Resour Res* **2018**, *54*, 4823-4848.
29. Xue, Y.; Forman, B.A.; Reichle, R.H. Estimating Snow Mass in North America Through Assimilation of Advanced Microwave Scanning Radiometer Brightness Temperature Observations Using the Catchment Land Surface Model and Support Vector Machines. *Water Resour Res* **2018**, *54*, 6488-6509.
30. Dechant, C.; Moradkhani, H. Radiance data assimilation for operational snow and streamflow forecasting. *Advances in Water Resources* **2011**, *34*, 351-364.
31. De Lannoy, G.J.M.; Reichle, R.H.; Arsenault, K.R.; Houser, P.R.; Kumar, S.; Verhoest, N.E.C.; Pauwels, V.R.N. Multiscale assimilation of Advanced Microwave Scanning Radiometer-EOS snow water equivalent and Moderate Resolution Imaging Spectroradiometer snow cover fraction observations in northern Colorado. *Water Resour Res* **2012**, *48*.
32. Charrois, L.; Cosme, E.; Dumont, M.; Lafaysse, M.; Morin, S.; Libois, Q.; Picard, G. On the assimilation of optical reflectances and snow depth observations into a detailed snowpack model. *Cryosphere* **2016**, *10*, 1021-1038.

33. Kim, E.; Gatebe, C.; Hall, D.; Newlin, J.; Misakonis, A.; Elder, K.; Marshall, H.P.; Hiemstra, C.; Brucker, L.; De Marco, E. NASA's SnowEx campaign: Observing seasonal snow in a forested environment. In Proceedings of 2017 IEEE International Geoscience and Remote Sensing Symposium (IGARSS); pp. 1388-1390.
34. Durand, M.; Kim, E.J.; Margulis, S.A. Quantifying Uncertainty in Modeling Snow Microwave Radiance for a Mountain Snowpack at the Point-Scale, Including Stratigraphic Effects. *Ieee T Geosci Remote* **2008**, *46*, 1753-1767, doi:10.1109/tgrs.2008.916221.
35. Proksch, M.; Matzler, C.; Wiesmann, A.; Lemmetyinen, J.; Schwank, M.; Lowe, H.; Schneebeli, M. MEMLS3&a: Microwave Emission Model of Layered Snowpacks adapted to include backscattering. *Geosci Model Dev* **2015**, *8*, 2611-2626.
36. Wiesmann, A.; Matzler, C. Microwave emission model of layered snowpacks. *Remote Sens Environ* **1999**, *70*, 307-316.
37. Benjamin, S.G.; Weygandt, S.S.; Brown, J.M.; Hu, M.; Alexander, C.R.; Smirnova, T.G.; Olson, J.B.; James, E.P.; Dowell, D.C.; Grell, G.A., et al. A North American Hourly Assimilation and Model Forecast Cycle: The Rapid Refresh. *Mon Weather Rev* **2016**, *144*, 1669-1694.
38. Blaylock, B.K.; Horel, J.D.; Liston, S.T. Cloud archiving and data mining of High-Resolution Rapid Refresh forecast model output. *Comput Geosci-Uk* **2017**, *109*, 43-50.
39. Xia, Y.L.; Mitchell, K.; Ek, M.; Sheffield, J.; Cosgrove, B.; Wood, E.; Luo, L.F.; Alonge, C.; Wei, H.L.; Meng, J., et al. Continental-scale water and energy flux analysis and validation for the North American Land Data Assimilation System project phase 2 (NLDAS-2): 1. Intercomparison and application of model products. *J Geophys Res-Atmos* **2012**, *117*.
40. Elder, K.; Brucker, L.; Hiemstra, C.; Marshall, H. SnowEx17 Community Snow Pit Measurements. Version: 2018.
41. Devonec, E.; Barros, A.P. Exploring the transferability of a land-surface hydrology model. *J Hydrol* **2002**, *265*, 258-282.
42. Bindlish, R.; Barros, A.P. Aggregation of digital terrain data using a modified fractal interpolation scheme. *Comput Geosci-Uk* **1996**, *22*, 907-917.
43. Liao, M.; Ana, P.B. GPM Ground Validation Reference Precipitation IPHEx. NASA Global Hydrology Resource Center DAAC, Huntsville, Alabama, U.S.A: 2019; undefined.
44. Nogueira, M.; Barros, A.P. Transient stochastic downscaling of quantitative precipitation estimates for hydrological applications. *J Hydrol* **2015**, *529*, 1407-1421.
45. Tao, K.; Barros, A.P. Using Fractal Downscaling of Satellite Precipitation Products for Hydrometeorological Applications. *J Atmos Ocean Tech* **2010**, *27*, 409-427.
46. Tao, J.; Barros, A.P. Multi-year atmospheric forcing datasets for hydrologic modeling in regions of complex terrain - Methodology and evaluation over the Integrated Precipitation and Hydrology Experiment 2014 domain. *J Hydrol* **2018**, *567*, 824-842.
47. Raleigh, M.S.; Livneh, B.; Lapo, K.; Lundquist, J.D. How Does Availability of Meteorological Forcing Data Impact Physically Based Snowpack Simulations?*. *J Hydrometeorol* **2016**, *17*, 99-120, doi:10.1175/jhm-d-14-0235.1.
48. National Academies of Sciences, E., and Medicine. *Thriving on our changing planet: A decadal strategy for Earth observation from space*; National Academies Press: 2019.
49. Yurchak, B.S. Effect of Snow Density Irregularities on Radar Backscatter from a Layered Dry Snow Pack. *Progress In Electromagnetics Research* **2014**, *59*, 181-191.
50. Oveisgharan, S.; Esteban-Fernandez, D.; Waliser, D.; Friedl, R.; Nghiem, S.; Zeng, X. Evaluating the Preconditions of Two Remote Sensing SWE Retrieval Algorithms over the US. *Remote Sens-Basel* **2020**, *12*, doi:10.3390/rs12122021.
51. Willmott, C.J.; Robeson, S.M.; Matsuura, K. A refined index of model performance. *Int J Climatol* **2012**, *32*, 2088-2094.